

Line formation in solar granulation

IV. [O I], O I and OH lines and the photospheric O abundance

Martin Asplund¹, Nicolas Grevesse^{2,3}, A. Jacques Sauval⁴, Carlos Allende Prieto⁵ and Dan Kiselman⁶

¹ Research School of Astronomy and Astrophysics, Mt. Stromlo Observatory, Cotter Rd., Weston, ACT 2611, Australia

² Centre Spatial de Liège, Université de Liège, avenue Pré Aily, B-4031 Angleur-Liège, Belgium

³ Institut d'Astrophysique et de Géophysique, Université de Liège, Allée du 6 août, 17, B5C, B-4000 Liège, Belgium

⁴ Observatoire Royal de Belgique, avenue circulaire, 3, B-1180 Bruxelles, Belgium

⁵ McDonald Observatory and Department of Astronomy, University of Texas, Austin, TX 78712-1083, USA

⁶ The Institute for Solar Physics of the Royal Swedish Academy of Sciences, AlbaNova University Centre, SE-106 91 Stockholm, Sweden

Accepted for Astronomy & Astrophysics

Abstract. The solar photospheric oxygen abundance has been determined from [O I], O I, OH vibration-rotation and OH pure rotation lines by means of a realistic time-dependent, 3D, hydrodynamical model of the solar atmosphere. In the case of the O I lines, 3D non-LTE calculations have been performed, revealing significant departures from LTE as a result of photon losses in the lines. We derive a solar oxygen abundance of $\log \epsilon_{\text{O}} = 8.66 \pm 0.05$. All oxygen diagnostics yield highly consistent abundances, in sharp contrast with the results of classical 1D model atmospheres. This low value is in good agreement with measurements of the local interstellar medium and nearby B stars. This low abundance is also supported by the excellent correspondence between lines of very different line formation sensitivities, and between the observed and predicted line shapes and center-to-limb variations. Together with the corresponding down-ward revisions of the solar carbon, nitrogen and neon abundances, the resulting significant decrease in solar metal mass fraction to $Z = 0.0126$ can, however, potentially spoil the impressive agreement between predicted and observed sound speed in the solar interior determined from helioseismology.

Key words. Convection – Line: formation – Sun: abundances – Sun: granulation – Sun: photosphere – Stars: atmospheres

1. Introduction

Oxygen is the most abundant element in the Universe with a non-Big Bang nucleosynthesis origin. As a consequence, oxygen plays a central role in many different fields of astrophysics ranging from supernova physics and galaxy evolution to dating stars and production of the light elements through cosmic ray spallation. Yet it appears that in many crucial objects for which accurate knowledge of the oxygen abundances is necessary the oxygen content is hotly debated. Recent disputes revolve around the overabundance of oxygen in metal-poor halo stars (see Asplund & García Pérez 2001; Nissen et al. 2002 and references therein), the Galactic radial abundance gradient (Rolleston et al. 2000; Cunha & Daflon 2003), and, astonishingly, the solar oxygen abundance. Partly these disagreements stem from differences in the adopted input data (e.g. gf -values, effective temperatures T_{eff} , surface gravities $\log g$) but more importantly they reflect the choice of spectral lines to derive the abundances using classical 1D stellar model atmospheres. In particular in the solar case, the freedom of parameters to ob-

tain consistency is very restricted yet the discrepancy is present in full.

Until recently the commonly adopted solar oxygen abundance was $\log \epsilon_{\text{O}} = 8.93 \pm 0.04$ ¹ (Anders & Grevesse 1989). This historically high abundance was suggested by analyses of the forbidden [O I] 630.0 nm line (Lambert 1978) as well as OH vibration-rotation and pure rotation lines in the infrared (Grevesse et al. 1984; Sauval et al. 1984) using the 1D hydrostatic Holweger-Müller (1974) semi-empirical model of the solar atmosphere and LTE line formation. On the other hand, a much lower abundance is indicated by the permitted high-excitation O I lines, most noteworthy the IR triplet at 777 nm, when employing the same model atmosphere with non-LTE line formation. This discrepancy of about 0.2 dex between different abundance indicators have often been blamed on over-estimated departures from local thermodynamic equilibrium (LTE) for the O I lines (Tomkin et al. 1992; Takeda 1994). Indeed, the LTE abundance of the triplet is close to the [O I] and OH-based abundance with the Holweger-Müller model. Such

Send offprint requests to: e-mail: martin@mso.anu.edu.au

¹ On the customary abundance scale defined as $\epsilon(X) = 10^{12} \cdot N(X)/N(\text{H})$

argumentation, however, ignores the available observational evidence such as the center-to-limb variation that the triplet is definitely not formed in LTE (Altrock 1968; Sedlmayr 1974; Kiselman 1993; Kiselman & Nordlund 1995). Uncertainties surround not only the O I lines but also the other indicators. The [O I] line is very weak and blended with a Ni I line (Lambert 1978; Reetz 1998; Allende Prieto et al. 2001). The OH lines are, like all molecules in the relevant temperature regime of the solar atmosphere, very temperature sensitive and therefore susceptible to surface inhomogeneities like granulation (Kiselman & Nordlund 1995; Asplund & García Pérez 2001), which are ignored in classical 1D model atmospheres. Unfortunately, no guidance regarding the solar oxygen abundance is available from meteorites, contrary to the situation for most other elements (Grevesse & Sauval 1998). Like carbon and nitrogen, oxygen is a highly volatile element which has partly escaped from the most primitive meteorites, the CI-chondrites, leaving only a fraction of the original amount (10%, 3% and 54% of C, N and O, respectively).

Recently, Allende Prieto et al. (2001) suggested a significant down-ward revision of the solar oxygen abundance to $\log \epsilon_{\text{O}} = 8.69 \pm 0.05$ based on a study of the [O I] 630.0 nm line using a time-dependent 3D hydrodynamical model of the solar atmosphere (Asplund et al. 2000b). Most of the 0.24 dex difference with the previous higher value is attributed to a previously ignored Ni I blend (-0.13 dex), although the difference between 3D and 1D models compounds the effect (-0.08 dex). In addition, a revision of the transition probability of the line causes a further 0.03 dex decrease. A similar low value was obtained by Holweger (2001) driven primarily by permitted O I lines: $\log \epsilon_{\text{O}} = 8.74 \pm 0.08$. This new low O abundance largely resolves another puzzling problem with the old high oxygen abundance, namely that the Sun is apparently oxygen-rich compared with the present-day local interstellar medium (e.g. Meyer et al. 1998; André et al. 2003) and nearby B stars (e.g. Cunha & Lambert 1994; Kilian et al. 1994; Sofia & Meyer 2001). Since the birth of the Sun some 4.5 Gyr ago, the gas in the solar neighborhood from which these hot stars have recently formed should have been further chemically enriched by nuclear-processed ejecta from dying stars. Several explanations like migration of the solar Galactic orbit have been proposed to address this conundrum but they may all be superfluous if the new low solar oxygen abundance is confirmed.

Relying solely on a single line for an as important quantity as the solar O abundance is no doubt highly unsatisfactory, in particular given the significant Ni blend of the [O I] 630.0 nm line. It is therefore clearly of importance to extend the work by Allende Prieto et al. (2001) to include also the O I and OH lines analysed with the same 3D hydrodynamical model atmosphere. Such a study is presented here, which firmly establishes the reality of the low solar photospheric oxygen abundance. It is noteworthy that for the first time ever the different line indicators give consistent results, which strongly supports the high degree of realism obtained with the new generation of 3D model atmospheres suggested by previous studies.

2. Analysis

2.1. Atomic and molecular data

[O I] lines: The gf -value of the [O I] 630.03 nm line has recently been revised to $\log gf = -9.717$ (Storey & Zeippen 2000), which we adopt here. This is a slight revision from the previously commonly adopted value of $\log gf = -9.75$ (Lambert 1978). The 630.03 nm feature has a non-negligible contribution from a Ni I line (Lambert 1968; Reetz 1998; Allende Prieto et al. 2001) which must be taken into account. Johansson et al. (2003) has very recently measured the transition probability of the Ni line and found $\log gf = -2.11$. However, since only the product $\epsilon_{\text{Ni}} \cdot gf$ enters the χ^2 -analysis of the [O I] 630.0 nm line profile fitting as a free parameter (Allende Prieto et al. 2001), this new value will not modify the derived O abundance but only the solar Ni abundance suggested by this one line. The isotopic splitting for the Ni line also determined by Johansson et al. (2003) is taken into account for the synthesis of the 630.03 nm line. The corresponding data for the weaker [O I] 636.37 nm line is $\log gf = -10.185$ (Storey & Zeippen 2000). In the analysis of this transition care must be exercised due to problematic blending of CN lines and a Ca I auto-ionization line at the wavelength of the [O I] 636.37 nm line.

O I lines: As described below, we chose to retain only six permitted O I lines (615.81, 777.19, 777.41, 777.53, 844.67 and 926.6 nm) for the abundance analysis to minimise the errors stemming from blends, uncertain gf -values, continuum placement and too weak spectral lines. The transition probabilities and lower level excitation potentials for the five lines were taken from the NIST database². The VALD database³ (Piskunov et al. 1995; Kupka et al. 1999) was consulted for radiative broadening and central wavelengths. Collisional broadening by H (commonly referred to as van der Waals broadening) was computed from the quantum mechanical theory of Anstee & O'Mara (1995), Barklem & O'Mara (1997) and Barklem et al. (1998). This removes the need for the conventional enhancement factors to the Unsöld (1955) classical recipe for collisional broadening. Some of the relevant line properties are listed in Table 2.

OH vibration-rotation and pure rotation lines: We selected the best 70 vibration-rotation lines of the (1,0), (2,1) and (3,2) bands as well as the best 127 pure rotation lines belonging to the 0-0, 1-1, 2-2 and 3-3 bands in the infrared solar spectrum. The dissociation energy of OH is very accurately known since quite a long time: $D_0(\text{OH}) = 4.392 \pm 0.005$ eV (Carlone & Dalby 1969). The molecular partition functions and equilibrium constants have been taken from Sauval & Tatum (1984). Lower level excitation potentials were adopted from Mélen et al. (1995). The gf -values were calculated by E. van Dishoeck (private communication) adopting the Electric Dipole Moment Function (EDMF) of Nelson et al. (1990). We checked that this EDMF leads to more consistent results than other calculated EDMFs. We note that this EDMF has also been selected by Goldman et al. (1998) in their recent data base for the OH X²II

² http://physics.nist.gov/cgi-bin/AtData/main_asd

³ <http://www.astro.uu.se/~vald>

ground state. A direct comparison of the gf -values with those of Goldman et al. (1998) reveal essentially identical results.

2.2. Observational data

For the analysis of the forbidden [O I] and permitted O I lines which are all located in the optical region (600–850 nm) the solar flux atlas of Kurucz et al. (1984) has been employed. This atlas has a signal-to-noise ratio in the optical of 200–3000, and a resolving power of about 500,000. Minor adjustments to the tabulated continuum level were made for the small wavelength regions directly surrounding the lines. For the 3D analysis, the oxygen abundances suggested by the individual lines were determined by profile fitting which is possible in view of the in general excellent agreement between predicted and observed line profiles in 3D (e.g. Asplund et al. 2000a,b,c). This is also the main reason why we employ flux profiles rather than the computationally less demanding disk-center intensity profiles for the oxygen lines: the agreement between predicted and observed profiles is slightly worse in intensity for the O I lines. Their very significant departures from LTE modify the intensity profiles more than the corresponding flux profiles. We emphasize, however, that very similar oxygen abundances are obtained for the O I and [O I] lines with flux and disk-center intensity profiles.

The OH vibration-rotation and pure rotation lines are located in the infrared. Our analysis has made use of the Spacelab-3 Atlas-3 ATMOS⁴ solar disk-center intensity IR observations recorded in November 1994 which are of better quality (i.e. less telluric absorption) than in the IR atlas (Farmer & Norton 1989; Farmer 1994). The relevant OH lines were identified and their equivalent widths measured (in milli-Kayser \equiv milli cm^{-1} , subsequently converted to the corresponding values in wavelength units [pm]).

Solar observations of the center-to-limb variation of several spectral lines, were carried out in October 22, 1997, with the Gregory Coudé Telescope (GCT) and its Czerny-Turner echelle spectrograph (Kneer et al. 1987) at the Observatorio del Teide (Tenerife, Spain). The observations of the O I 777 nm triplet have an estimated resolving power $R = 86,000$. Scattered light was estimated to amount to about 6% and corrected by comparing the observations at the center of the disk with the Fourier Transform Spectrograph atlas by Brault & Neckel (1987). The observations were done for disk-positions $\mu = 1.00, 0.97, 0.87, 0.71, 0.50$ and 0.17 . The observed center-to-limb variations of the equivalent widths for the O I 777 nm triplet are very similar to those measured by Müller et al. (1968) and Altrock (1968) except at the lowest μ -point, where our data is less steep. More details of the observations and data reduction are provided in a separate paper (Allende Prieto et al., in preparation).

2.3. 3D hydrodynamical solar model atmosphere

We employ the same 3D, time-dependent, hydrodynamical model of the solar atmosphere, which has previously been ap-

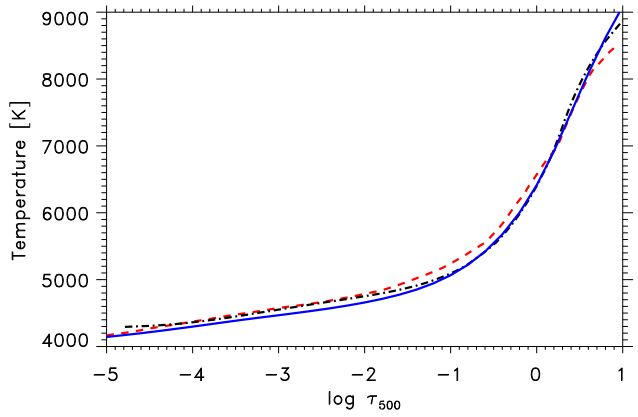


Fig. 1. The temporally and spatially averaged temperature structure of the 3D solar surface convection simulation (solid line) used for the 3D spectral line formation. The spatial averaging has been performed over surfaces of the same continuum optical depths at 500 nm. Note that the actual 3D simulation extends to much greater optical depths than shown here. Also shown are the temperature structures for the 1D Holweger-Müller (1974) semi-empirical solar atmosphere (dashed line) and the 1D MARCS (Asplund et al. 1997) theoretical solar atmosphere (dashed-dotted line).

plied to solar spectrum line formation for the present series of articles (Asplund 2000; Asplund et al. 2000b,c; Asplund et al. 2004b,c) and elsewhere (Allende Prieto et al. 2001, 2002a, b; Asplund 2004). This new generation of model atmospheres has proven to be highly realistic, successfully reproducing a wide range of observational constraints, such as spectral line shapes, shifts and asymmetries (Paper I; Allende Prieto et al. 2002a), helioseismology (Rosenthal et al. 1999; Stein & Nordlund 2001), flux distribution and limb-darkening (Asplund et al. 1999b) and granulation properties (Stein & Nordlund 1998). It is clear that the new 3D solar model atmosphere represents a significant improvement over existing 1D hydrostatic LTE models.

In short, the equations of mass, momentum and energy conservation together with the simultaneous solution of the 3D radiative transfer equation along nine inclined directions have been solved on a Eulerian mesh with $200 \times 200 \times 82$ grid-points: for the spectral line formation calculation this was subsequently interpolated to a $50 \times 50 \times 82$ grid. The physical dimension (6 Mm horizontally and 3.8 Mm vertically with about 1 Mm located above $\tau_{500} = 1$) of the numerical grid were sufficiently large to cover $\gtrsim 10$ granules simultaneously and extends to nearly adiabatic conditions in the bottom. Periodic horizontal and open vertical boundary conditions have been employed. The simulations make use of the state-of-the-art MHD equation-of-state (Mihalas et al. 1988) and comprehensive opacities, including line opacities (Gustafsson et al. 1975 with subsequent updates; Kurucz 1993). The effects of line-blanketing is accounted for through opacity binning (Nordlund 1982) which is a form of multi-group opacities. Some relevant properties of the temporally and spatially (over surfaces of

⁴ <http://remus.jpl.nasa.gov/atmos/ftp.at3.sun.html>

Table 1. Temporally and spatially averaged atmospheric stratification of the 3D solar surface convection simulation used for the 3D spectral line formation presented here: temperature, density, gas pressure, electron pressure and vertical velocity (positive velocities inward) as well as their rms-scatter. The spatial averaging has been performed over surfaces of the same continuum optical depths at 500 nm. Note that the original 3D model extends significantly above and below the optical depths for which the mean structure has been interpolated to and tabulated. We emphasize that it is not possible to explain all 3D effects by a comparison of such an averaged 3D model with existing 1D models due to the absence of atmospheric inhomogeneities.

$\log \tau_{500\text{nm}}$	T [K]	ΔT_{rms} [K]	ρ [kg/m ³]	$\Delta \rho_{\text{rms}}$ [kg/m ³]	P_{gas} [Pa]	$\Delta P_{\text{gas,rms}}$ [Pa]	P_e [Pa]	$\Delta P_{e,\text{rms}}$ [Pa]	v_z [km/s]	$\Delta v_{z,\text{rms}}$ [km/s]
-5.00	4143	153	8.28E-13	8.39E-14	2.34E+01	3.16E+00	2.09E-03	4.56E-04	0.06	1.53
-4.80	4169	161	1.09E-12	1.16E-13	3.10E+01	4.40E+00	2.73E-03	6.39E-04	0.04	1.46
-4.60	4198	167	1.43E-12	1.55E-13	4.10E+01	5.89E+00	3.58E-03	8.65E-04	0.03	1.37
-4.40	4230	172	1.88E-12	1.99E-13	5.41E+01	7.54E+00	4.69E-03	1.14E-03	0.03	1.29
-4.20	4263	176	2.47E-12	2.44E-13	7.13E+01	9.30E+00	6.11E-03	1.47E-03	0.03	1.22
-4.00	4297	180	3.21E-12	2.90E-13	9.34E+01	1.12E+01	7.94E-03	1.88E-03	0.03	1.14
-3.80	4332	184	4.16E-12	3.40E-13	1.22E+02	1.32E+01	1.03E-02	2.39E-03	0.03	1.07
-3.60	4368	188	5.36E-12	3.99E-13	1.58E+02	1.55E+01	1.32E-02	3.03E-03	0.03	1.02
-3.40	4402	192	6.89E-12	4.69E-13	2.04E+02	1.81E+01	1.69E-02	3.84E-03	0.03	0.96
-3.20	4435	197	8.82E-12	5.56E-13	2.63E+02	2.11E+01	2.16E-02	4.88E-03	0.03	0.92
-3.00	4467	202	1.13E-11	6.75E-13	3.38E+02	2.46E+01	2.74E-02	6.22E-03	0.04	0.89
-2.80	4500	207	1.44E-11	8.38E-13	4.33E+02	2.89E+01	3.48E-02	7.93E-03	0.04	0.86
-2.60	4535	212	1.83E-11	1.06E-12	5.55E+02	3.43E+01	4.41E-02	1.01E-02	0.04	0.84
-2.40	4571	217	2.32E-11	1.35E-12	7.10E+02	4.11E+01	5.59E-02	1.30E-02	0.05	0.84
-2.20	4612	221	2.95E-11	1.72E-12	9.08E+02	4.98E+01	7.12E-02	1.67E-02	0.06	0.85
-2.00	4658	224	3.75E-11	2.16E-12	1.16E+03	6.05E+01	9.12E-02	2.14E-02	0.06	0.88
-1.80	4711	225	4.77E-11	2.68E-12	1.49E+03	7.46E+01	1.17E-01	2.75E-02	0.07	0.93
-1.60	4773	221	6.05E-11	3.27E-12	1.92E+03	9.27E+01	1.53E-01	3.50E-02	0.08	1.00
-1.40	4849	213	7.65E-11	3.94E-12	2.46E+03	1.17E+02	2.00E-01	4.41E-02	0.09	1.10
-1.20	4944	196	9.61E-11	4.83E-12	3.14E+03	1.52E+02	2.67E-01	5.44E-02	0.10	1.22
-1.00	5066	170	1.20E-10	6.20E-12	4.01E+03	2.05E+02	3.61E-01	6.57E-02	0.10	1.38
-0.80	5221	141	1.47E-10	8.30E-12	5.08E+03	2.83E+02	5.02E-01	8.04E-02	0.10	1.56
-0.60	5420	126	1.79E-10	1.12E-11	6.40E+03	3.89E+02	7.44E-01	1.24E-01	0.09	1.76
-0.40	5676	154	2.13E-10	1.57E-11	7.97E+03	5.27E+02	1.27E+00	3.48E-01	0.08	1.99
-0.20	6000	227	2.46E-10	2.40E-11	9.72E+03	7.63E+02	2.64E+00	1.20E+00	0.06	2.22
0.00	6412	332	2.70E-10	3.65E-11	1.14E+04	1.15E+03	6.71E+00	4.08E+00	-0.01	2.47
0.20	6919	481	2.82E-10	5.17E-11	1.28E+04	1.66E+03	1.98E+01	1.47E+01	-0.13	2.71
0.40	7500	645	2.85E-10	6.63E-11	1.39E+04	2.21E+03	5.69E+01	4.38E+01	-0.27	2.91
0.60	8084	759	2.83E-10	7.78E-11	1.49E+04	2.74E+03	1.33E+02	9.44E+01	-0.39	3.05
0.80	8619	813	2.81E-10	8.64E-11	1.58E+04	3.26E+03	2.52E+02	1.60E+02	-0.49	3.14
1.00	9086	817	2.79E-10	9.30E-11	1.67E+04	3.77E+03	4.08E+02	2.30E+02	-0.56	3.19
1.20	9478	782	2.79E-10	9.82E-11	1.76E+04	4.30E+03	5.90E+02	2.92E+02	-0.61	3.20
1.40	9797	719	2.82E-10	1.02E-10	1.86E+04	4.83E+03	7.82E+02	3.36E+02	-0.64	3.18
1.60	10060	644	2.87E-10	1.06E-10	1.97E+04	5.37E+03	9.84E+02	3.64E+02	-0.66	3.13
1.80	10290	573	2.96E-10	1.08E-10	2.09E+04	5.89E+03	1.21E+03	3.95E+02	-0.67	3.06
2.00	10493	509	3.09E-10	1.10E-10	2.25E+04	6.38E+03	1.46E+03	4.36E+02	-0.67	2.96

same optical depths) averaged 3D solar simulation is listed in Table 1, limited to the optical depth range relevant for spectrum formation. The mean temperature structure $\langle T(\tau_{500}) \rangle_\tau$ is shown in Fig. 1. We emphasize, however, that the atmospheric inhomogeneities are also important for the spectrum formation, which has been fully taken into account in the 3D line formation. The reader is referred to Stein & Nordlund (1998) and Paper I for further details of the construction of the 3D solar model atmosphere.

For comparison purposes, we have also performed identical calculations employing two well-used 1D hydrostatic models of the solar atmosphere: the semi-empirical Holweger-Müller (1974) model and a theoretical, LTE, line-blanketed MARCS model (Asplund et al. 1997). Their temperature struc-

tures $T(\tau_{500})$ are compared with the mean 3D stratification in Fig. 1.

2.4. 3D LTE spectral line formation

Equipped with the 3D hydrodynamical solar model atmosphere, 3D spectral line formation calculations have been performed for the [O I], O I and OH lines. The radiative transfer equation has been solved under the assumption of LTE for the ionization and excitation with the source function being equal to the local Planck function ($S_\nu = B_\nu$). Comprehensive background continuous opacities (Gustafsson et al. 1975; Asplund et al. 1997) and an equation-of-state which accounts for excitation, ionization and molecule formation of the most important

elements (Mihalas et al. 1988) have been used, with instantaneous chemical equilibrium being assumed for the molecule formation. For the [O I] and O I lines flux profiles have been computed from a solution of the radiative transfer equation along 17 different inclined directions ($N_\mu = N_\varphi = 4$ plus the vertical) making use of the periodic horizontal boundaries. For the OH lines disk-center intensity profiles have been obtained. The flux profiles have been disk-integrated assuming a solar rotation velocity of 1.8 km s^{-1} . All 3D LTE spectral line formation computations have been carried out for 100 snapshots covering 50 min of solar time after which temporal and spatial averaging have been performed. For each line, a local continuum flux/intensity has been computed with the same procedure as for the line profiles, enabling proper normalized profiles. Each line has been calculated with three different abundances differing by 0.2 dex from which the profile with the correct equivalent width (OH lines) or line shape ([O I] and O I lines) has been interpolated. Extensive testing has shown that the procedure yields correct abundances to within 0.01 dex. No micro- and macroturbulence enter the 3D calculations as the self-consistently computed convective velocities and temperature inhomogeneities induce Doppler shifts which give rise to excellent agreement between observed and predicted line shapes without such additional line broadening which is always needed in standard 1D analyses (Asplund et al. 2000b; Asplund 2000; Allende Prieto et al. 2002a).

The corresponding 1D calculations based on the MARCS and Holweger-Müller model atmospheres have been performed using exactly the same codes and procedures as for the 3D case, with the exception that a microturbulence of $\xi_{\text{turb}} = 1.0 \text{ km s}^{-1}$ has been adopted. To investigate the sensitivities of the lines to this parameter, all 1D profiles have also been computed using $\xi_{\text{turb}} = 1.5 \text{ km s}^{-1}$.

2.5. 3D non-LTE spectral line formation for O I

It is well-known that the high-excitation permitted O I lines suffer from significant departures from LTE (Sedlmayr 1974; Kiselman 1991; Kiselman & Nordlund 1995; Kiselman 2001). It is therefore paramount to investigate these non-LTE effects also in 3D and include non-LTE abundance corrections in the final analysis of the O I lines. The 3D non-LTE line formation calculations have been performed with MULTI3D (Botnen 1997; Botnen & Carlsson 1999; Asplund et al. 2003a), which iteratively solves the rate equations simultaneously with the radiative transfer equation assuming statistical equilibrium ($dN_i(x, y, z)/dt = 0$). Due to the very computationally demanding nature of 3D non-LTE line formation calculations, compromises must be made in terms of the number of snapshots for which the non-LTE solution is obtained. From the 50 min time sequence for which the 3D LTE line formation calculations were performed, two typical snapshots were chosen which were sufficiently separated in time to be considered independent. To improve the numerical accuracy in the non-LTE case, the $50 \times 50 \times 82$ grid used for the 3D LTE spectrum synthesis were interpolated to a finer $50 \times 50 \times 100$ grid extending down to at least $\log \tau_{500} = 2$ for all vertical columns. Test

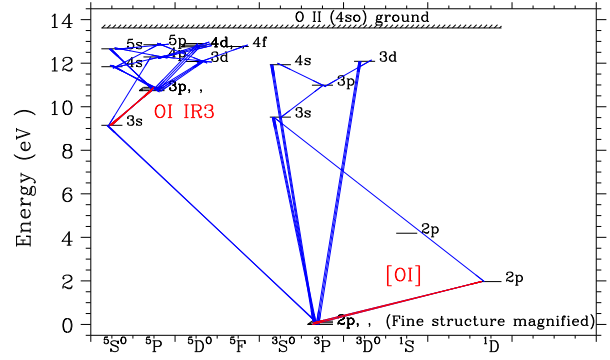


Fig. 2. Grotrian term-diagram of the employed 23-level O model atom with 22 bound states of O I and the ground state of O II. The forbidden [O I] 630.0 and 636.3 nm lines originate from the $2p^4 \ 3P$ ground state, while the O I 777 nm triplet is between the high-excitation $3s \ 5S^o$ and $3p \ 5P$ levels. The 43 bound-bound transitions are drawn. All O I levels are connected by bound-free transitions with the ground state of O II but are not shown for clarity

calculations were also performed on a smaller $25 \times 25 \times 100$ grid, yielding very similar results. Tests with different vertical depth-scales yielded insignificant differences in the resulting non-LTE abundance corrections.

The radiative transfer equation was solved for 24 outgoing inclined rays using a short characteristic technique and making use of the periodic horizontal boundary conditions. The line broadening caused by Doppler shifts introduced by the convective motions in the hydrodynamical model atmospheres was taken into account. No microturbulence or macroturbulence thus enter the 3D calculations. The background continuous opacities and equation-of-state were computed with the Uppsala opacity package (Gustafsson et al. 1975 and subsequent updates). For completeness we note that this equation-of-state is not the same as used in the construction of the 3D model atmosphere but very similar in the relevant temperature regime. The effect of this difference will however be minute since both the LTE and non-LTE line profiles for the two selected snapshots used for the derivation of the non-LTE abundance corrections are both based on the same input physics in all aspects, as described in detail below. This non-LTE abundance correction is then applied to the LTE estimates based on the whole 100 snapshot long temporal sequence, which indeed have the same equation-of-state as the 3D model atmosphere. Finally, we note that all four codes employed in this study (3D hydrodynamics, 3D LTE line formation, MULTI for 1D non-LTE line formation and MULTI3D for 3D non-LTE line formation) rely on the Uppsala opacity package for continuous opacities.

Line-blanketing using data from Kurucz (1993) were taken into account for the photo-ionization rates but was found to be insignificant for the present case. The main effect of the line blanketing on the statistical equilibrium of metals that do not contribute significantly to the blanketing is generally

through the reduction of the available photoionizing UV photons, but with such a large ionization energy, oxygen is insensitive to changes in the UV solar flux (see, e.g. Allende Prieto et al. 2003). Flux profiles were constructed from the angle-dependent intensity profiles. The corresponding LTE-profiles for the selected snapshots were also produced with MULTI3D using the same model atom but with all collisional probabilities multiplied by very large factors to ensure full thermalization of all rates. The non-LTE abundance corrections were estimated by computing both the non-LTE and LTE cases for three abundances differing by 0.2 dex and interpolating the non-LTE line strengths reproducing the LTE equivalent widths from the profile fitting. Both 3D snapshots gave the same non-LTE correction to within 0.01 dex. Similarly robust results were obtained in the case of Li (Asplund et al. 2003a). Hence, while the line strengths vary somewhat from snapshot to snapshot following differences in the granulation pattern, the non-LTE abundance corrections stay essentially the same.

The O model atom consists of 22 O I levels and the ground state of O II. The term diagram of the adopted model atom is presented in Fig. 2. In total 43 bound-bound and 22 bound-free radiative transitions were included together with electron collisional excitation and ionization. Charge transfer reactions from the ^3P ground states have been taken into account; large charge transfer cross-sections for excited states as for Li I (Barklem et al. 2003) are not expected for O. We note that removing all charge transfer reactions only implies < 0.005 dex changes to the computed non-LTE abundance corrections for the Sun, reflecting the very minor influence of all ionization rates. Inelastic collisions with H for excitation and ionization were not accounted for, as the available laboratory measurements and detailed calculations strongly suggests that the classical Drawin (1968) formula over-estimates the collisional rates by at least three orders of magnitude in the cases of Li and Na (Fleck et al. 1991; Belyaev et al. 1999; Barklem et al. 2003; see also discussion in Kiselman 2001). Unfortunately the specific case of O has not yet been investigated but there are no compelling reasons on atomic physics grounds to expect a qualitatively different behaviour for O compared with Li and Na in this respect. Furthermore, center-to-limb variation observations of the O I triplet suggests that the Drawin recipe over-estimates the collisional efficiency (Allende Prieto et al., in preparation). The adopted model atom is similar to the atom employed in the study of Kiselman (1993). We have verified that even an equivalent two-level atom yields very similar non-LTE abundance corrections as the full O atom. With the expected main non-LTE effect being photon losses in the line itself for the IR triplet our adopted atom is extensive enough to produce reliable results (Kiselman 1993). The 3D non-LTE abundance corrections for the O I lines employed in the present study are listed in Table 2.

Due to their high excitation potential ($\chi_{\text{exc}} > 9$ eV), the O I lines are formed in deep atmospheric layers with a significant temperature contrast between the warm upflowing gas (granules) and the cool downflows (intergranular lanes), as exemplified in Fig. 3. It is clear that the main effect of the non-LTE line formation is a general strengthening of the O I IR triplet over the whole granulation pattern. In this sense, the

Table 2. The computed non-LTE abundance corrections for the three different model atmospheres. The departures from LTE have been estimated using MULTI3D (Botnen 1997 Asplund et al. 2003a) for the 3D case and with MULTI (Carlsson 1986) for the 1D model atmospheres, in all cases using the same 23-level model atom.

line		χ_{exc}	$\log gf$	$\Delta(\log \epsilon_{\text{O}})$		
[nm]		[eV]		3D	HM	MARCS
[O I]:						
630.03	$^3\text{P} - ^1\text{D}$	0.00	-9.72	+0.00	+0.00	+0.00
636.67	$^3\text{P} - ^1\text{D}$	0.02	-10.19	+0.00	+0.00	+0.00
O I:						
615.81	$^5\text{P} - ^5\text{D}^{\circ}$	10.74	-0.30	-0.03	-0.05	-0.03
777.19	$^5\text{S}^{\circ} - ^5\text{P}$	9.15	+0.37	-0.27	-0.29	-0.24
777.41	$^5\text{S}^{\circ} - ^5\text{P}$	9.15	+0.22	-0.24	-0.27	-0.23
777.53	$^5\text{S}^{\circ} - ^5\text{P}$	9.15	+0.00	-0.20	-0.24	-0.20
844.67	$^3\text{S}^{\circ} - ^3\text{P}$	9.52	+0.01	-0.20	-0.25	-0.21
926.60	$^5\text{P} - ^5\text{D}^{\circ}$	10.74	+0.82	-0.08	-0.11	-0.08

non-LTE line formation is largely a 1D problem: quite similar results are obtained for O I if the non-LTE calculations are restricted to 1.5D (i.e. ignoring all non-vertical radiative transfer) rather than 3D. The depression of the line source function thus operates qualitatively similarly in both up- and downflows, although the details differ somewhat. As seen in Fig. 3, the largest 3D non-LTE effects are in fact seen in the intergranular lanes, which however, also house the smallest non-LTE effects in regions immediately adjacent to edge-brightened granules. Fig. 4 shows the line strength of the O I 777.41 nm line as a function of the local continuum intensity. Again, the non-LTE and LTE behaviour are qualitatively similar for the triplet with the main difference being a shift in overall equivalent widths for the same abundance. The lack of a clear difference between the two cases in this respect is in sharp contrast to the case of Li (Kiselman 1997; Uitenbroek 1998; Asplund et al. 2003a), where the shapes of the LTE and non-LTE loci differ markedly. It will therefore be difficult to confirm the 3D non-LTE line formation modelling through observations of spatially resolved O I lines, as is possible for elements like Li and Fe (Kiselman & Asplund 2001). As expected, the [O I] lines are formed perfectly in LTE, as seen in Fig. 4.

The 1D non-LTE line formation with the MARCS and the Holweger-Müller model atmospheres has been studied with the code MULTI (Carlsson 1986) using the same model atom as in the 3D case. The structures of the MULTI3D and MULTI codes are very similar with the exceptions of the geometry and the use of long characteristics for the solution of the radiative transfer with MULTI. In particular, the subroutines for the background opacities and equation-of-state calculations are identical in the two cases. The non-LTE abundance corrections for the two 1D model atmospheres are presented in Table 2. It is worth noting the similarity between the non-LTE corrections in 1D and 3D in the case of O I lines in the Sun, in particular for the theoretical MARCS model. Although detailed results require 3D calculations, non-LTE computations in 1D model atmospheres are of great value to explore whether a given spectral line is prone to departures from LTE, at least at solar metallicities. At low

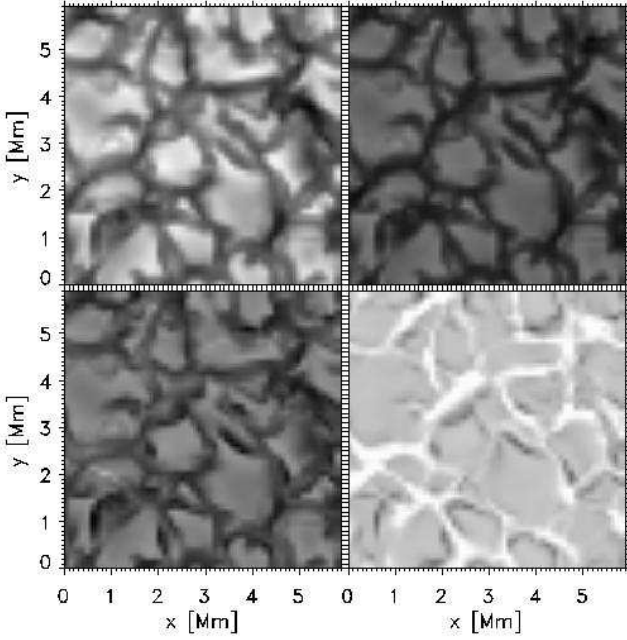


Fig. 3. The granulation pattern in one of the solar snapshots seen in disk-center continuum intensity at 777 nm (*upper left panel*) and equivalent width of the O I 777.41 nm line in LTE (*upper right panel*) and non-LTE (*lower left panel*); the equivalent width images have the same relative intensity scale to emphasize the overall difference in line strengths. Also shown is the ratio of the non-LTE and LTE equivalent widths (*lower right panel*).

metallicities, the temperature structure is sufficiently different between 1D and 3D model atmospheres that one can expect significantly larger non-LTE effects in 3D for many elements (Asplund et al. 1999a, 2003a).

3. The solar photospheric O abundance

3.1. Forbidden [O I] lines

The ability of the 3D hydrodynamical solar model atmosphere to very accurately predict detailed spectral line shapes and asymmetries without invoking additional ad-hoc broadening like micro- and macroturbulence represents a major advantage in abundance analyses, as obvious from the analysis of the forbidden [O I] 630.0 nm line. It has long been suspected that the line is indeed blended by a weak Ni I line (Lambert 1968). Due to the until recently very uncertain transition probability of the Ni line, it has been difficult to ascertain its overall contribution to the 630.0 nm feature and hence the solar O abundance. Lambert (1978) estimated the Ni contribution to be $0.02 \text{ pm} = 0.2 \text{ mÅ}$, while the use of the theoretical gf -value ($\log gf = -1.74$) of Kurucz (1993) for the Ni line would imply a very small left-over contribution for the [O I] line using the solar Ni abundance derived from other isolated lines. The 3D model atmosphere can be used to estimate the necessary Ni line contribution in order to reproduce the shape of the observed feature. Without taking into account the Ni line, the pre-

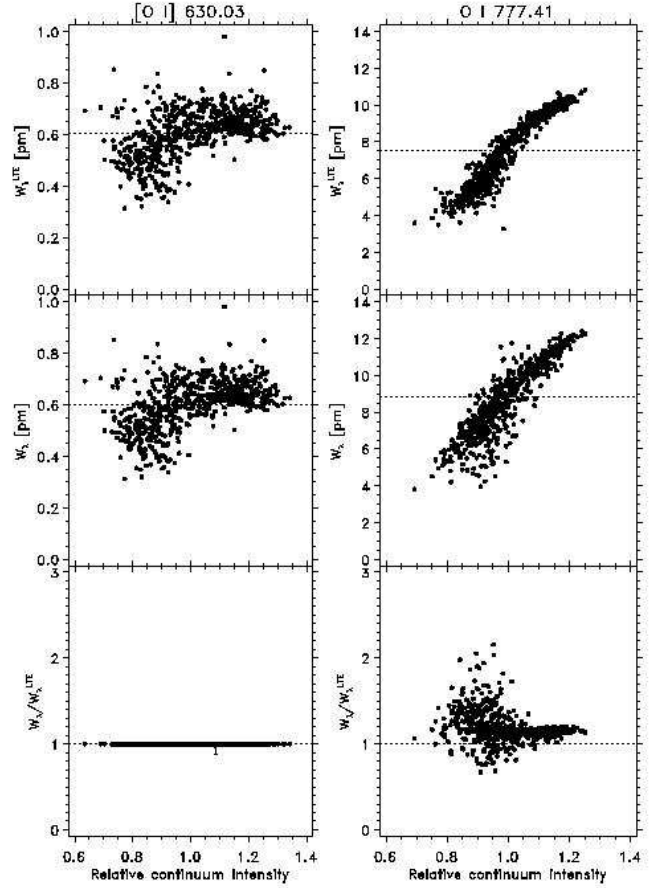


Fig. 4. Predicted intensity ($\mu = 1.0$) equivalent widths of the [O I] 630.03 nm (*left panel*) and O I 777.41 nm (*right panel*) lines across the granulation pattern in LTE (*upper panel*) and non-LTE (*middle panel*). Both cases are computed for $\log \epsilon_{\text{O}} = 8.90$ for the two lines. The mean intensity equivalent widths are denoted by horizontal lines. Also shown are the ratios of the non-LTE and LTE equivalent widths (*lower panel*), with the horizontal lines representing the average ratio for the two lines. As expected, the [O I] line is in perfect LTE while the O I line shows significant departures from LTE. Note that for clarity only a selection of the vertical atmospheric columns are shown.

dicted [O I] line has completely the wrong central wavelength and a line shape different from observed (see Fig. 1 in Allende Prieto et al. 2001), a discrepancy which is far worse than seen in similar 3D calculations for any other unblended line.

From a χ^2 -analysis of the flux profile of the [O I] 630.0 nm line, Allende Prieto et al. (2001) concluded that the solar O abundance is $\log \epsilon_{\text{O}} = 8.69 \pm 0.05$ based on the same 3D model atmosphere as employed here. Since then, Johansson et al. (2003) have measured a new gf -value for the blending Ni I line and details of its isotopic splitting. Johansson et al. have modelled the shape of the Ni I line at the lab with two major components, due to the isotopes ^{60}Ni and ^{58}Ni , which contribute 94.3 % of the *terrestrial* abundance (Rosman & Taylor 1998). Although the exact gf -value is inconsequential for our

purposes (only the product $\epsilon_{\text{Ni}} \cdot gf$ enters the analysis⁵), the additional line broadening from isotopic splitting changes the line profile of the Ni line somewhat and therefore also slightly the χ^2 -analysis. The center of gravity of the line is also mildly changed from the value used by Allende Prieto et al. (630.0339 nm; Litzén et al. 1993) to 630.0341 nm. Taking this into account, however, only results in a 0.005 dex higher abundance than without the isotopic splitting. We therefore still arrive at $\log \epsilon_{\text{O}} = 8.69 \pm 0.05$ (Table 3). The same abundance is obtained when using disk-center intensity profiles instead of flux profiles.

Adopting the theoretical line strength of only the [O I] 630.0 nm line as judged by the 3D analysis (0.36 pm=3.6 mÅ for disk-center intensity and 0.43 pm for flux) for the 1D calculations using the Holweger-Müller and the MARCS model atmospheres, we find $\log \epsilon_{\text{O}} = 8.77 \pm 0.05$ and $\log \epsilon_{\text{O}} = 8.73 \pm 0.05$, respectively. It should be noted, however, that it is not possible to accurately evaluate the Ni line contribution to the feature based only on a 1D analysis (Lambert 1968; Reetz 1998) due to the absence of intrinsic line asymmetries and the poor overall agreement between predicted and observed line profiles with 1D hydrostatic models. For a long time, it was therefore simply assumed that the Ni line was unimportant, leading to a much larger derived solar O abundance (e.g. Lambert 1978; Sauval et al. 1984): $\log \epsilon_{\text{O}} \simeq 8.90$ for the Holweger-Müller model using the new gf -value of the [O I] 630.0 nm line adopted here. This clearly illustrates the importance of having a realistic model atmosphere which adequately describes the intrinsic line shapes and asymmetries due to the convective motion and temperature inhomogeneities.

As mentioned above, the analysis of the [O I] 636.3 nm line is hampered by blending CN lines. In addition, the line is located in the midst of a Ca I auto-ionization line. The main blending CN line is the Q₂ (25.5) 10-5 line with a center wavelength of 636.3776 nm, which is very close to the wavelength of the [O I] line: 636.3792 nm. In addition, the P₁ (53.5) 8-3 CN line at 636.3846 nm is blending in the red wing. The contributions of these CN lines have been determined from spectrum synthesis using the parameters for the two bands determined from other CN lines as well as for theoretical values. Together the two CN lines are estimated to have an equivalent width of 0.050 ± 0.005 pm (flux), where the uncertainty reflects the different possible choices of transition probabilities of the CN lines. This leaves 0.14 pm (1.4 mÅ) to be attributed to the [O I] line. In terms of abundance this corresponds to $\log \epsilon_{\text{O}} = 8.67$ when analysed with the 3D hydrodynamical solar model atmosphere (Table 3). For the Holweger-Müller and the MARCS model atmospheres, we find $\log \epsilon_{\text{O}} = 8.75$ and $\log \epsilon_{\text{O}} = 8.71$, respectively.

The [O I] 557.73 nm line is not considered here since it is badly blended by a C₂ doublet whose exact contribution is very difficult to ascertain (Lambert 1978).

3.2. Permitted O I lines

Of the 20 odd observable lines attributed to O I in the wavelength range 500 – 1400 nm, unfortunately only a few are suitable for accurate abundance analysis besides the two forbidden lines discussed above. The O I 615.68 nm line is definitely blended as are five lines at wavelengths greater than 900 nm (926.27, 974.15, 1130.24, 1316.39 and 1316.49 nm). The heavy blending preventing their use has been verified by detailed 3D spectrum synthesis, as the shapes of clean lines are very well predicted by the new generation of 3D hydrodynamical model atmosphere (e.g. Asplund et al. 2000b; Asplund 2000; Allende Prieto et al. 2002a). The two very faint ($W_{\lambda} < 0.1$ pm) lines at 645.44 and 700.19 nm are not considered here because of their weakness and their uncertain theoretical gf -values. The 844.63 nm line is affected by uncertainties in the continuum placement and blending while the 976.07 nm lacks appropriate atomic data. This leaves only the familiar O I IR triplet at 777 nm (777.19, 777.41, 777.53 nm) and the even more high-excitation 615.81 nm line. In addition, we include the 844.67 nm line but with half weight compared with the other lines as it is partly blended and located in a region with a less well-determined continuum. The latter line also shows similarly large non-LTE abundance corrections as the IR triplet, i.e. $\simeq -0.2$ dex. Finally, we include the 926.60 nm line, also with half weight as the line is blended in the red wing by a telluric H₂O line. As a consequence, it is not possible to use the flux atlas to derive the abundance. While the Brault & Neckel (1987) disk-center intensity solar atlas⁶ still shows a prominent telluric feature, the Liège Jungfraujoch (Delbouille et al. 1973) disk-center atlas⁷ has a diminished problem with telluric absorption in this wavelength region. For this line only we therefore fit the disk center intensity profile instead of the flux profile for this particular line. Note that the line consists in fact of three components at 926.5827, 926.5927 and 926.6007 nm with $\log gf = -0.72, +0.13$ and $+0.71$, respectively, which have been taken into account for the theoretical calculations.

The derived O I-based abundances have been obtained from the temporally and spatially averaged 3D LTE flux profiles and taking into account the departures from LTE calculated in Sect. 2.5. We note that almost identical abundances are derived when relying on disk-center intensity profiles instead. The 3D LTE profiles have been computed for 100 snapshots corresponding to 50 min solar time for in total 17 different rays. Through a comparison with the observed profiles, the individual abundances best reproducing the line shapes and strengths for the different O I lines were estimated. To these 3D LTE abundances, the 3D non-LTE abundance corrections presented in Table 2 are added. The final 3D non-LTE abundances are found in Table 3. Due to the in general poorer agreement between predicted and observed profiles with 1D model atmospheres, the same profile fitting technique is not as easily employed in the 1D cases. Instead, the theoretical equivalent widths in 3D computed with the thus obtained abundances have been used as “observed” equivalent widths to be reproduced with the two

⁵ In principle, one should re-determine the solar Ni abundance using other Ni lines with our new 3D model atmosphere in order to evaluate whether the new gf -value for the Ni I 630.0 nm line is indeed consistent with the solar Ni abundance. We postpone such a study to a later time as it is not crucial for our conclusions here.

⁶ ftp.hs.uni-hamburg.de/pub/outgoing/FTS-atlas

⁷ http://bass2000.obspm.fr/solar_spect.php

Table 3. The derived solar oxygen abundance as indicated by forbidden [O I] and permitted O I lines. The results for the O I lines include the non-LTE abundance corrections presented in Table 2 which have been computed specifically for the three different model atmospheres

line [nm]	χ_{exc} [eV]	$\log gf$	3D ^a	W_{λ}^b [pm]	HM ^c	MARCS ^c
[O I]:						
630.03	0.00	−9.72	8.69	0.43	8.77	8.73
636.37	0.02	−10.19	8.67	0.14	8.75	8.71
O I:						
615.81	10.74	−0.30	8.62	0.41	8.77	8.77
777.19	9.15	+0.37	8.64	7.12	8.60	8.71
777.41	9.15	+0.22	8.65	6.18	8.60	8.71
777.53	9.15	+0.00	8.66	4.88	8.62	8.71
844.67 ^d	9.52	+0.01	8.60	3.52	8.58	8.67
926.60 ^e	10.74	+0.82	8.65	3.62	8.68	8.69

^a The abundances derived using the 3D model atmosphere have been obtained from profile fitting of the observed lines.

^b The predicted flux equivalent widths (except for 926.60 nm which is for disk center intensity) with the 3D model atmosphere using the best fit abundances shown in the fourth column.

^c The derived abundances with the Holweger-Müller (1974) and the MARCS (Asplund et al. 1997) 1D hydrostatic model atmospheres in order to reproduce the equivalent widths presented in the fifth column. Note that for the [O I] 630.03 nm line use of 1D models prevents accurate estimation of the significant Ni I line blending (Allende Prieto et al. 2001). Without the 3D results at hand, a significantly larger O abundance of $\log \epsilon_{\text{O}} \simeq 8.9$ would therefore be obtained.

^d Half weight compared with the other lines is assigned to the 844.67 nm line due to problems with blending and continuum placement.

^e Half weight compared with the other lines is assigned to the 926.60 nm line due to problems with blending and continuum placement. Note that the line in fact consists of three components, which has been taken into account in the spectrum synthesis. In order to minimize the effect of the telluric H₂O blend, the disk-center intensity profile has been fitted, and hence the tabulated equivalent width is for the intensity rather than for flux profile as for all other lines here.

different 1D model atmospheres. This ensures that the same line strengths are obtained in both 1D and 3D and isolates the impact of the new generation of 3D solar model atmosphere compared with existing 1D models. As in 3D, the 1D non-LTE abundance corrections individually computed for the two 1D model atmospheres have been added to the results presented in Table 3.

It is noteworthy that the 3D non-LTE abundances in Table 3 show very gratifying agreement in spite of the very significant differences in non-LTE abundance corrections between the different lines. In particular, the 615.81 nm and 926.60 nm lines show a small departure from LTE (−0.03 dex and −0.08 dex, respectively, in terms of abundance) while the other four O I lines have substantial non-LTE effects (−0.20... − 0.27 dex), yet the final non-LTE abundances agree to within 0.06 dex. While the non-LTE effect on the 615.81 nm line is small, the

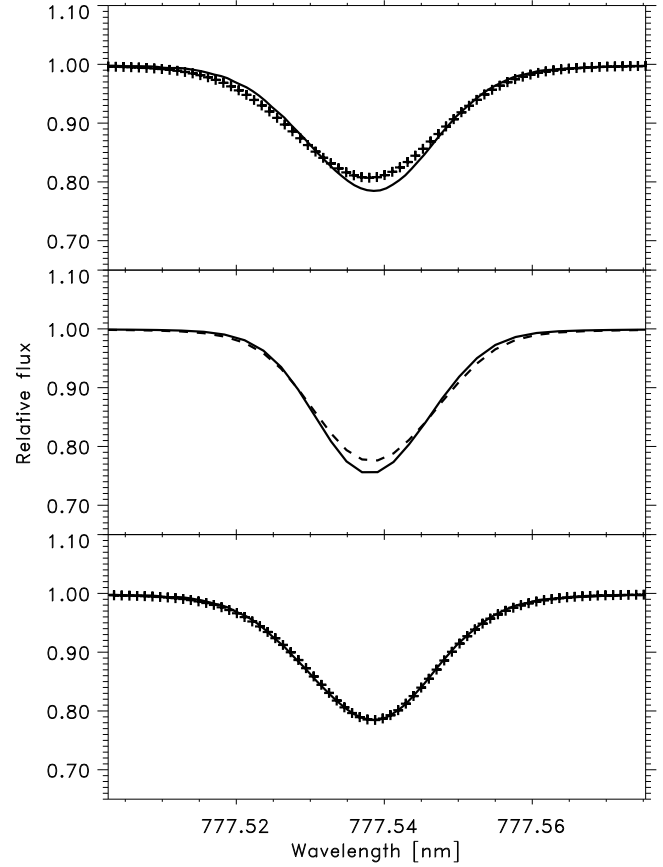


Fig. 5. *Upper panel:* The temporally and spatially averaged LTE flux profile from the 3D model atmosphere (+) together with the observed profile (solid line) for the O I 777.53 nm line. The theoretical profile has been computed with $\log \epsilon_{\text{O}} = 8.86$ and convolved with a Gaussian corresponding to the instrumental resolution. Clearly the 3D LTE profile lacks effects of departures from LTE in the line formation. *Middle panel:* The 3D non-LTE (solid line) and the 3D LTE (dashed line) line profiles computed for one snapshot with MULTI3D (Botnen 1997 Asplund et al. 2003a). The 3D non-LTE profile has been computed with $\log \epsilon_{\text{O}} = 8.70$ while for the LTE case an abundance of $\log \epsilon_{\text{O}} = 8.90$ was adopted. In terms of equivalent widths the two profiles have the same line strengths. *Lower panel:* The temporally and spatially averaged 3D profile taking into account departures from LTE (+) shown together with the observed profile (solid line). The 3D non-LTE profile has been obtained by multiplying the 3D LTE profile in the upper panel with the ratio of non-LTE and LTE profiles presented in the middle panel. While not a perfect substitute for the temporally averaged 3D non-LTE profile it nevertheless shows a very encouraging agreement with observations. The observed line profiles have been corrected for the solar gravitational redshift of 633 m s^{-1} .

3D LTE effect (3D LTE - 1D LTE) is significantly larger than for the other O I lines in view of its very high excitation potential ($\chi_{\text{exc}} = 10.74 \text{ eV}$) and large atmospheric formation depth. In sharp contrast, with the Holweger-Müller model atmosphere the 615.81 nm line implies a significantly larger abundance

than the 777 nm triplet by $\gtrsim 0.15$ dex. With the MARCS model atmosphere the agreement is better but still significantly poorer than in 3D. It should be noted however that the here performed 1D analyses benefit greatly from the 3D analysis. The equivalent widths estimated from the 3D line profile fitting are much more accurate than those directly measured from the observed profiles using for example Gaussian or Voigt functions as commonly done due to the asymmetries of the lines and the presence of blends. We interpret the excellent agreement in 3D as yet additional evidence for a very high degree of realism in the 3D model atmosphere and 3D line formation modelling.

Not only are the derived abundances very consistent in 3D, the predicted profiles also closely resemble the observed profiles, as evident from Fig. 5. While the 3D LTE profiles are broader and have a too pronounced blue asymmetry compared with what the observations indicate, including the 3D non-LTE effects results in almost perfect matches with the observed profiles for the O I IR triplet. It should be noted that due to computational constraints the 3D non-LTE calculations can only be performed for a small number of snapshots, preventing proper temporally averaged 3D non-LTE profiles as can be straightforwardly achieved in 3D LTE. Instead the effects of departures from LTE on the 3D profiles have been included by multiplying the temporally averaged 3D LTE profiles with the ratios of the 3D non-LTE and 3D LTE profiles computed with MULTI3D for the two selected snapshots. This procedure is justified since the differences in 3D non-LTE abundance corrections between different snapshots are expected to be small (Asplund et al. 2003a), as also confirmed by specific calculations for O. Thereby the final 3D non-LTE profiles incorporate the effects of the Doppler shifts introduced by convective motions and solar oscillations, which in 1D is assumed to be replaced with a depth-independent and isotropic micro- and macroturbulence. The agreement between predicted and observed profiles is in general significantly poorer in 1D even when including an individually optimized macroturbulence parameter. The excellent agreement between observed and predicted profiles for the 3D non-LTE calculations is a very strong support for our modelling.

Further support for the 3D model atmosphere and the 3D non-LTE line formation modelling is obtained from a comparison of the center-to-limb variation of the O I 777 nm triplet. As discussed in detail in Kiselman & Nordlund (1995), the observed dependence of line strength on disk location μ is much more shallow than predicted when assuming LTE regardless of whether a 3D or 1D model atmosphere is employed. In contrast, the non-LTE case reproduces the observed behaviour very nicely, at least when not including the very large cross-sections for inelastic collisions with H implied by the classical Drawin (1968) formula (see discussion in Kiselman 2001). Not surprisingly given the similarity in the employed 3D solar model atmospheres and the robustness of the non-LTE effects as discussed in Sect. 2.5, we confirm the findings of Kiselman & Nordlund (1995). In this respect, our much more extended model atom compared with their two-level approach is of little consequence, as the dominant non-LTE effect is a depression of the line source function due to escape of 777 nm line photons (Kiselman 1993). As shown in Fig. 6, the 3D non-LTE

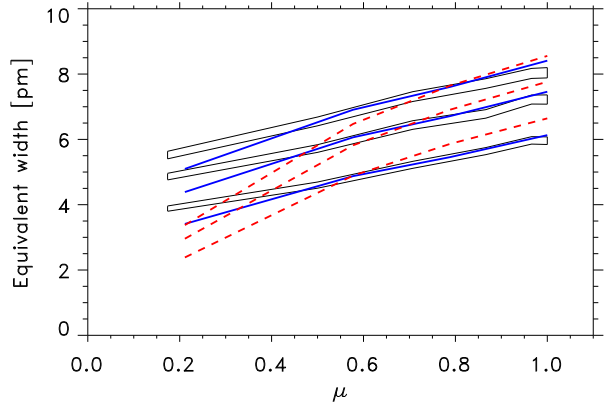


Fig. 6. The observed center-to-limb variations of the equivalent widths of the O I 777 nm triplet are shown as bands with estimated internal errors. The solid lines denote the average of two snapshots of the theoretical 3D non-LTE results for the three lines, while the dashed lines represent the corresponding 3D LTE case. The here shown 3D LTE curves are very similar to the average of all 100 snapshots computed with the same 3D line formation code used for the calculations of the [O I] and OH lines. As two snapshots are insufficient to yield an accurate abundance estimate, the 3D non-LTE results have been interpolated to $\log \epsilon_{\text{O}} \approx 8.7$ to overlap with the observational estimates to high-light the excellent agreement in the center-to-limb variation in 3D non-LTE. In all cases, the LTE curves correspond to a 0.2 dex higher abundance than the non-LTE cases. Clearly, LTE fails to reproduce the observational evidence, while the non-LTE calculations are in good agreement.

results for the center-to-limb variations of the triplet agree very well with the observational evidence, in particular for $\mu \geq 0.5$. We note that an even more impressive agreement for $\mu < 0.5$ would have been achieved had we relied on the only, to our knowledge at least, previously published center-to-limb variation observations of the triplet by Müller et al. (1968) and Altrock (1968). Our new solar observations are in excellent accordance with those of Müller et al. (1968) and Altrock (1968), except for the data points at $\mu = 0.17$, the only disk position with $\mu < 0.5$ we acquired spectra for.

3.3. OH vibration-rotation lines

The availability of high-resolution solar atlases in the IR with exquisite signal-to-noise ratio such as the here employed ATMOS atlas enables the use of the OH vibration-rotation around $3 \mu\text{m}$ and the OH pure rotation lines beyond $9 \mu\text{m}$ as oxygen abundance indicators (Grevesse et al. 1984; Sauval et al. 1984). The high-quality observed spectrum combined with the relatively small amount of problematic blending in the relevant wavelength regions ensures that highly precise equivalent widths (initially in milli-Kayser = milli-cm^{-1} due to the nature of the solar atlas and subsequently converted to pm) of the OH lines can be measured. For the analysis of the OH $X^2\Pi$ vibration-rotation lines we utilise 70 lines in the P_i -branch of

the (1,0) and (2,1) bands with $N'' < 20$; the Q and R lines fall in wavelength regions completely dominated by CO_2 and H_2O . The (1,0) and (2,1) lines are all weak and hence insensitive to the non-thermal broadening (convective motions in 3D and microturbulence in 1D). Due to the large number of lines, our OH-based oxygen abundances are determined using the measured equivalent widths with the assumption of LTE in the line formation. For vibration-rotation lines like these, LTE is likely an excellent approximation (Hinkle & Lambert 1975). The issue of non-equilibrium molecule formation for OH has garnered relatively little attention in the literature but the available evidence suggests that it is not a serious worry for the OH lines in the Sun at least (Sánchez Almeida et al. 2001; Asensio Ramos et al. 2003).

The resulting O abundances with the 3D model atmosphere show encouragingly small scatter and without any trends with neither wavelength, excitation potential nor line strength, as clear from Fig. 7. Considering the high degree of temperature sensitivity of OH molecule formation and the minute fraction of oxygen tied up in OH, this excellent agreement strongly suggests that the temperature structure in the 3D model atmosphere is very close to reality in the relevant atmospheric depth interval (typical mean optical depth of line formation $\log \tau_{500} \approx -1.4$ in the case of the Holweger-Müller model. The concept of typical line formation depth is of course less well-defined in the case of 3D models). Giving equal weights to all 70 lines, the average of the individual abundances yields $\log \epsilon_{\text{O}} = 8.61 \pm 0.03$.

A similar analysis based on the 1D Holweger-Müller model atmosphere gives a significantly larger abundance: $\log \epsilon_{\text{O}} = 8.87 \pm 0.03$. While the scatter is only marginally larger than in 3D, there are disturbing trends in oxygen abundances as function of wavelength and excitation potential (Fig. 8); these trends are clearly inter-related as the low excitation lines have shorter wavelengths. It should also be noted that there is a significant trend with line strengths when using equivalent widths measured in wavenumber units rather than wavelengths. The relatively strong trend with excitation potential is particularly revealing, implying that the temperature structure of the Holweger-Müller model is inappropriate. In fact, the same conclusion led Grevesse & Sauval (1998) to experiment with a modified temperature structure in order to remove the existing trends but thereby also affecting the mean OH-based oxygen abundance. In this respect, the 1D MARCS model atmosphere is performing better. The resulting trends are barely significant (Fig. 9) and the scatter is very similar to the 3D case. The MARCS-based abundance is $\log \epsilon_{\text{O}} = 8.74 \pm 0.03$.

3.4. OH pure rotation lines

The pure rotational lines of OH $X^2\Pi$ were first identified in the solar atlas by Goldman et al. (1981, $v = 0$), Blatherwick et al. (1982, $v = 1$ and $v = 2$) and Sauval et al. (1984, $v = 3$). Goldman et al. (1983) and Sauval et al. (1984) have advocated for their use as a prime abundance indicator of the solar oxygen abundance given the large number of clean lines beyond $9\mu\text{m}$. Our analysis utilises 127 of the weakest OH pure

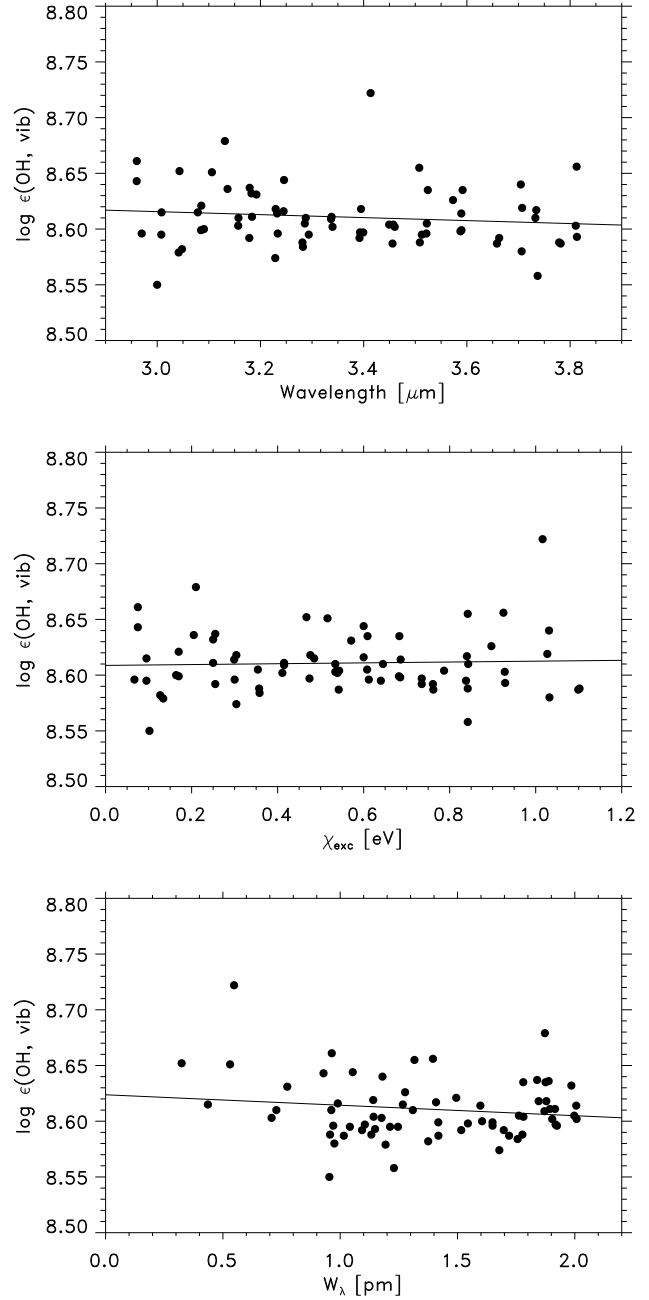


Fig. 7. The derived solar oxygen abundance (filled circles) from OH vibration-rotation lines using the 3D hydrodynamical time-dependent simulation of the solar atmosphere (Asplund et al. 2000b) as a function of wavelength, lower level excitation potential and line strength (in pm). The solid lines denote least-square-fits giving equal weights to all lines.

rotation lines belonging to the $v = 0$, $v = 1$, $v = 2$, and $v = 3$ states with $N'' = 23 - 43$, whose equivalent widths have been measured from the ATMOS solar IR atlas. Care has been exercised to only consider OH lines minimally affected by telluric absorption. While the equivalent widths and line depths for the pure rotation lines are in general smaller than for the vibration-rotation lines, the pure rotation lines are partly saturated since they are formed in significantly higher atmo-

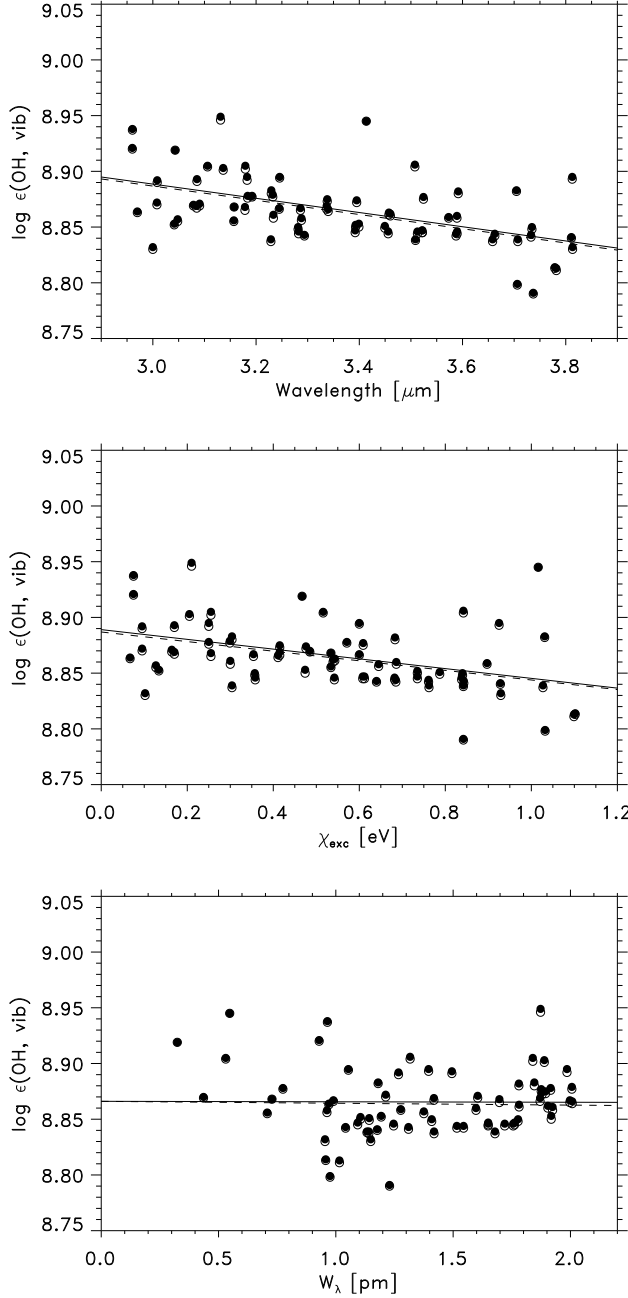


Fig. 8. Same as Fig. 7 but using the Holweger-Müller (1974) semi-empirical model atmosphere and a microturbulence of $\xi_{\text{turb}} = 1.0 \text{ km s}^{-1}$ (filled circles with solid lines denoting least-square-fits). The open circles and dashed lines correspond to a larger microturbulence ($\xi_{\text{turb}} = 1.5 \text{ km s}^{-1}$)

spheric layers (typical mean optical depth of line formation $-2.0 \lesssim \log \tau_{500} \lesssim -1.6$ in the case of the Holweger-Müller model). Hence the pure rotation lines are sensitive to the convective Doppler shifts (supposedly represented by microturbulence in 1D analyses) in addition to the temperature sensitivity normal for all molecules.

The equivalent width-based O abundances derived with the 3D model atmosphere show a small scatter, in particular for the lines with $W_\lambda = 1.5 - 10 \text{ pm}$. Due to observational prob-

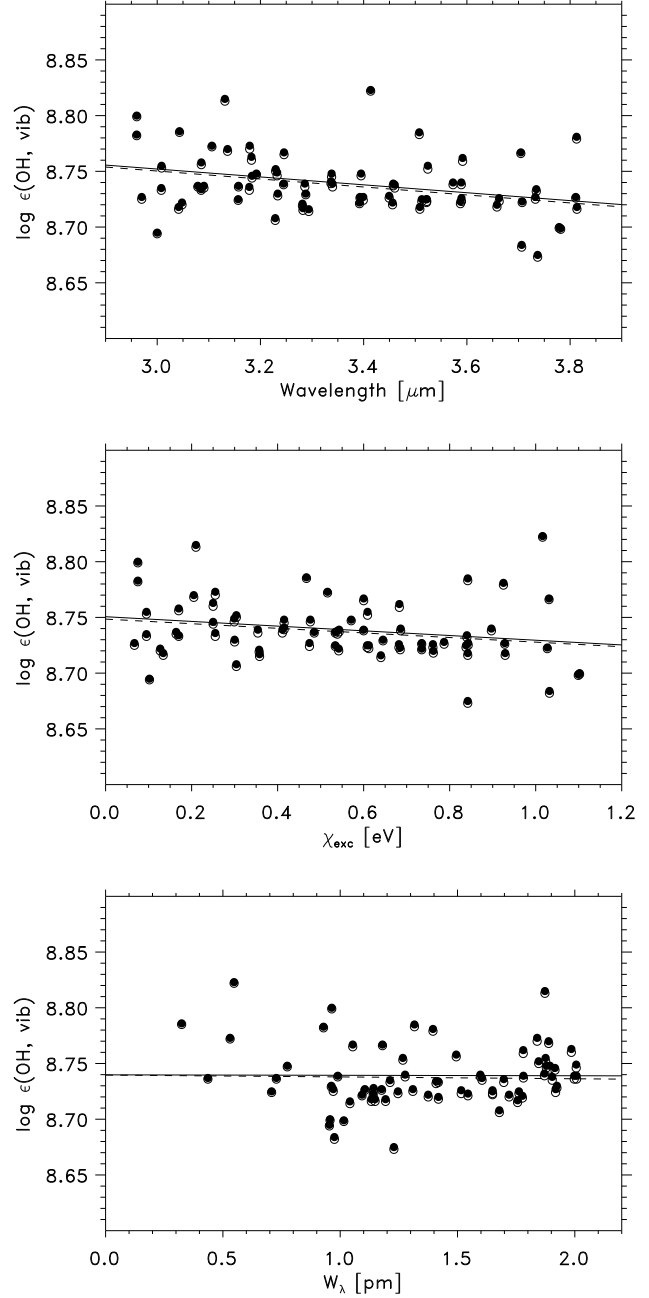


Fig. 9. Same as Fig. 7 but using a theoretical MARCS model atmosphere (Asplund et al. 1997) and a microturbulence of $\xi_{\text{turb}} = 1.0 \text{ km s}^{-1}$ (filled circles with solid lines denoting least-square-fits). The open circles and dashed lines correspond to a larger microturbulence ($\xi_{\text{turb}} = 1.5 \text{ km s}^{-1}$)

lems in accurately measuring the line strengths of the weakest lines, the scatter increases significantly for $W_\lambda < 1.5 \text{ pm}$. However, there are distinct trends with excitation potential and line strength for lines with $\chi_{\text{exc}} < 2 \text{ eV}$ and $W_\lambda > 10 \text{ pm}$, as seen in Fig. 10. These two trends are directly related since the lowest excitation lines are also the strongest. It is expected that the realism of the 3D model atmosphere starts to deteriorate towards higher atmospheric layers, in particular due to the employed radiative transfer treatment (total radiative heat-

ing/cooling determined by relatively few lines, lack of non-LTE effects, no consideration of Doppler shifts for the energy balance etc). These lines are also sensitive to the atmospheric velocity field. Less weight should therefore be placed on the stronger rotational lines. In the following, the analysis is restricted to the pure rotation lines with $W_\sigma = 1.5 - 10$ pm. Giving equal weight to these 69 lines results in $\log \epsilon_O = 8.65 \pm 0.02$.

We have also performed corresponding calculations with the MARCS and Holweger-Müller 1D model atmospheres (Figs. 12 and 11). The 1D analysis using the MARCS model atmosphere produces even more spectacular trends with excitation potential and line strengths with almost 0.2 dex higher abundance for the strongest lines compared with the weakest lines (Fig. 12). Adopting instead a high microturbulence of $\xi_{\text{turb}} = 1.5 \text{ km s}^{-1}$ instead of the standard $\xi_{\text{turb}} = 1.0 \text{ km s}^{-1}$ only goes about half-way in resolving the problems. Since such a high microturbulence is inconsistent with similar analyses of other species, we conclude that the temperature structure in these high atmospheric layers in the MARCS model is clearly inappropriate for the analysis of OH pure rotation lines. The average abundance for the same 69 lines as for the 3D analysis is $\log \epsilon_O = 8.83 \pm 0.02$. In this respect, the Holweger-Müller (1974) model is performing remarkably well with essentially no trends with the standard microturbulence of $\xi_{\text{turb}} = 1.0 \text{ km s}^{-1}$ and a very small scatter (Fig. 11). This is somewhat surprising given the problems encountered for the OH vibration-rotation lines with the same model atmosphere (Sect. 3.3). However, the pure rotation lines are formed in higher layers than the vibration-rotation lines (typically $-2.0 \lesssim \log \tau_{500} \lesssim -1.6$ and $\log \tau_{500} \simeq -1.4$, respectively, in the case of the Holweger-Müller model). The average abundance with the Holweger-Müller model is $\log \epsilon_O = 8.82 \pm 0.01$.

As mentioned above, it is slightly surprising that the Holweger-Müller model performs better than the 3D model for the pure rotation lines while the opposite is true for the vibration lines. The main effects must reside in the differences in temperature structure and/or velocity field (convection in 3D and microturbulence in 1D). The mean temperature stratifications differ in the relevant atmospheric layers, as illustrated in Fig. 1. It should be noted that the continuum optical depth scale at $3 \mu\text{m}$ (typical wavelengths for vibration lines) is very similar to that of 500 nm , while the continuum optical depth unity at $10 \mu\text{m}$ (typical for rotation lines) occurs at $\tau_{500} \approx -1.3$. This also causes a reversal of the granulation pattern when viewed at these long IR wavelengths: the bright (warm) material is located above the intergranular lanes and the dark (cool) material lays above the normal granules (see Fig. 1 in Kiselman & Nordlund 1995). Since the typical line formation depths differ for the two types of OH lines, it is possible to remove the abundance trends present in Fig. 10 without tampering with the excellent consistency achieved in Fig. 7 by slightly decreasing the temperatures outside $\tau_{500} \approx -1.6$. According to test calculations, the necessary temperature modifications are relatively small and fully within the uncertainties of the 3D temperature structure given the inherent approximations for the energy balance in these high atmospheric layers. The main problem appears to be the relative fine-tuning of the temperature

Table 4. The derived solar oxygen abundance as indicated by forbidden [O I], permitted O I lines, OH vibration-rotation line and OH pure rotation lines. The results for the O I lines include the non-LTE abundance corrections presented in Table 2. The quoted uncertainties only reflect the line-to-line scatter for the different types of O diagnostics while no doubt the total error is dominated by systematic errors.

lines	$\log \epsilon_O$		
	3D	HM	MARCS
[O I]	8.68 ± 0.01	8.76 ± 0.02	8.72 ± 0.01
O I	8.64 ± 0.02	8.64 ± 0.08	8.72 ± 0.03
OH vib-rot	8.61 ± 0.03	8.87 ± 0.03	8.74 ± 0.03
OH rot	8.65 ± 0.02	8.82 ± 0.01	8.83 ± 0.03

alterations necessary in order not to perturb the vibration lines. It is also possible that the resolution of the discrepancies can be found in underestimated temperature inhomogeneities in the OH line forming region with the present 3D model. A detailed comparison of observed and predicted *absolute* disk-center intensities is expected to be able to shed further light on this issue. While the strongest rotation lines are sensitive to the velocity field, the required changes make this a rather implausible solution according to various test calculations.

3.5. Summary

As seen above and summarised in Table 4, the different oxygen diagnostics used for the present study yield very consistent results when analysed with the 3D hydrodynamical solar model atmosphere. Clearly the situation is much less satisfactory when relying on classical 1D model atmospheres. We see no compelling reason to prefer or exclude any of the individual abundance indicators as the results are in all cases quite convincing. The quoted errors in Table 4 only reflect the line-to-line scatter (standard deviation rather than standard deviation of the mean as occasionally used for solar analyses) for the different types of lines. Using these standard deviations, the weighted mean becomes $\log \epsilon_O = 8.66 \pm 0.02$. However, the total error budget is most certainly dominated by systematic errors rather than statistical. Possible such sources include the atmosphere model (in particular the temperature structure), the continuous opacity (due perhaps to non-LTE effects on the H^- molecule) and non-LTE effects on the line and molecule formation. To evaluate systematic errors is notoriously difficult. An attempt of doing so can be achieved by a comparison of the abundances implied by the different indicators, which in the 3D case suggests that the remaining systematic errors are under reasonable control given the very different types of line formation processes involved and their widely different temperature sensitivities. A reasonable estimate would be to assign an uncertainty of ± 0.05 dex on the derived solar oxygen abundance. We therefore arrive at our best estimate of the solar oxygen abundance as:

$$\log \epsilon_O = 8.66 \pm 0.05.$$

4. The solar photospheric Ne and Ar abundances

The solar abundances of neon and argon are also directly affected by the new solar abundance of oxygen. Since spectral lines of Ne and Ar do not show up in the solar photospheric spectrum, their solar abundances have to be deduced from coronal matter. Oxygen, neon and argon particles are present in the solar wind as well as in solar energetic particles (SEP). As they are high FIP (First Ionisation Potential) elements they are not subject to fractionation affecting the low FIP elements in coronal matter. From the observed accurate SEP ratios, $\text{Ne/O} = 0.152 \pm 0.004$ and $\text{Ar/O} = (3.3 \pm 0.2) \cdot 10^{-3}$ (Reames 1999; these values agree with the somewhat less accurate solar wind data as well as with local galactic ratios derived from hot stars and nebulae) we deduce revised values of the solar abundances of Ne and Ar: $\log \epsilon_{\text{Ne}} = 7.84 \pm 0.06$ and $\log \epsilon_{\text{Ar}} = 6.18 \pm 0.08$ respectively. These values are again much smaller than the previously recommended values of 8.08 and 6.40, respectively, in Grevesse & Sauval (1998). The quoted errors account both for the measurement uncertainty in the element ratios in SEP and the estimated systematic error in the solar O abundance.

5. Comparison with previous studies

The derived solar oxygen abundances from the different indicators presented in Sect. 3 are particularly noteworthy for two reasons: the significantly lower O abundance by as much as 0.25 dex compared with previously commonly adopted values (Anders & Grevesse 1989; Grevesse & Sauval 1998), and the excellent agreement for all different features, in stark contrast to what is achieved with 1D model atmospheres. In particular the latter fact is a very strong argument in favour of the new generation of 3D hydrodynamical model atmosphere and their application to accurate abundance analyses.

In spite of their weakness, the forbidden [O I] 630.0 and 636.3 nm lines have often been advocated to be the superior O abundance indicators, in particular the former line (Lambert 1978). As both lines originate from the ground state, their line formations are guaranteed to be exceedingly well approximated by LTE as verified by our non-LTE calculations. Until recently, it was believed that the contribution from the blending Ni I 630.0 nm line was negligible, leading to an oxygen abundance of $\log \epsilon_{\text{O}} \simeq 8.9$ with the Holweger-Müller semi-empirical model atmosphere (Lambert 1978; Sauval et al. 1984; Holweger 2001). Strong support for this high abundance has come from analyses of the OH vibration-rotation (Grevesse et al. 1984) and pure rotation lines (Sauval et al. 1984), which show an impressively small scatter between different OH lines using the Holweger-Müller model. Together this led to the conclusion that the solar O abundance is $\log \epsilon_{\text{O}} = 8.93 \pm 0.03$ (Anders & Grevesse 1989). Since then the OH-based abundance has gradually come down by 0.1 dex in view of new preliminary analyses using a Holweger-Müller model atmosphere with a slightly modified temperature stratification to remove existing trends with excitation potential and line strength (Grevesse & Sauval 1998, 1999) and improved *gf*-values and measured equivalent widths. In the meantime, it has become

clear that the Ni I blend for the [O I] 630.0 nm line may not be insignificant after all. Reetz (1998) made a very comprehensive investigation using both flux and intensity solar atlases at different disk locations in an attempt to constrain the Ni contribution. While no unanimous conclusion could be reached, Reetz concluded that the Ni line could affect the results so much that the solar O abundances may be as low as $\log \epsilon_{\text{O}} = 8.75$ when analysed with the Holweger-Müller model. A more precise estimate of the Ni line contribution was obtained by Allende Prieto et al. (2001) by employing the same 3D hydrodynamical solar model atmosphere as used here. In terms of abundance it was found that properly taking the Ni line into account will lower the O abundance by about 0.13 dex. In comparison, the impact of moving from the classical Holweger-Müller 1D model atmosphere to a 3D model was less important in this case, 0.08 dex, but the two effects compound each other by going in the same direction. Together with a new *gf*-value (same as used here), Allende Prieto et al. (2001) obtained $\log \epsilon_{\text{O}} = 8.69 \pm 0.05$. The work presented here builds on the success of this study but extends it greatly by also performing similar calculations for the other O diagnostics. It is always worrisome when a result rests entirely on only one spectral line, in particular when the implication in terms of derived abundance is as profound as in this case and the line itself is significantly blended.

While both the [O I] and OH lines for long pointed towards a high solar O abundance, the permitted high-excitation O I lines were causing severe problems, in particular the IR triplet at 777 nm. It is well-known that the triplet is susceptible to departures from LTE, which increases the line strength and thus decreases the derived abundance. The exact magnitude of this non-LTE effect depends on the recipe, if any, for excitation by inelastic collisions with H. The exact choice of model atmosphere and other details of the model atom play a smaller role in this respect. The essentials of the line formation process of the triplet lines are in fact very well described even with a two-level approach in as far as the main non-LTE effect is photon-losses in the line itself, causing the line source function to deviate from the Planck value (Kiselman 1993). A smaller contribution from a slight change in the line opacity also modulates the result however. Without accounting for H-collisions, the non-LTE abundance corrections for these lines are about -0.2 dex for the Sun, leading to a solar O abundance of $\log \epsilon_{\text{O}} \simeq 8.7$ (Kiselman 1993). Due to the large discrepancy in the non-LTE case with the [O I] and OH results, many authors have argued that the non-LTE calculations are faulty. Indeed the LTE-abundance is close to those provided by the other diagnostics, providing in some people's eyes a mean to *calibrate* the poorly known H-collisions (Tomkin et al. 1992; Takeda 1994). By necessity, such a procedure requires the H-collisions to be very large, often even larger than the classical Drawin (1968) recipe for such processes, thus enforcing efficient thermalization of the line and a result close to the LTE-expectation. It is important to realise, however, that the available laboratory and theoretical calculations unambiguously suggest that the Drawin recipe over-estimates the H-collisions by about three orders of magnitude in the so far only studied cases of Li and Na (Fleck et al. 1991; Belyaev et al. 1999; Barklem et al. 2003).

If the same conclusions hold for O then the H-collisions are completely negligible in the solar case. Furthermore, center-to-limb variations of the predicted LTE-profiles (or those obtained from non-LTE calculations with Drawin-like H-collisions) differ markedly from the observational evidence, as seen in Fig. 6 (see also Kiselman & Nordlund 1995).

The root of the problem with 1D analyses has therefore been the poor agreement between the O abundances estimated from the [O I] and OH lines on the one hand and the O I lines on the other; with the Ni-induced downward revision of the [O I]-based abundance this statement must be modulated however. In an important paper, Kiselman & Nordlund (1995) attempted to resolve this long-standing discrepancy through a pioneering 3D analysis of the O I triplet, the [O I] 630.0 nm line and a few OH vibration-rotation and pure rotation lines. They used a similar but less sophisticated 3D model atmosphere compared to the one employed here and restricted the calculations to only two different snapshots. A noteworthy finding of their study was that it may be possible to reconcile the different abundance indicators in a proper 3D analysis since the [O I] and OH lines became stronger than in the Holweger-Müller model atmosphere while the opposite was true for the triplet as indicated by an equivalent two-level non-LTE calculation. Due to the restricted numerical resolution and temporal coverage, they were unable to perform an accurate abundance analyses for the lines, but they concluded that “*the solar oxygen abundance could very well be less than 8.80*”. Our 3D model atmosphere covering some 100 snapshots over a 50 min solar-time sequence with an improved temperature structure and extension to greater heights, allows us to derive significantly more accurate abundances and finally settle the issue.

Recently, Holweger (2001) has independently re-visited the solar O abundance using the [O I] 630.0 nm and O I lines; he did not study molecular lines. Holweger used the old gf -value for the forbidden line and neglected the Ni-blend and consequently found a high oxygen abundance: $\log \epsilon_{\text{O}} = 8.92$ using the Holweger-Müller model. His seven permitted lines suggested a significantly lower value, which, together with non-LTE abundance corrections, yielded $\log \epsilon_{\text{O}} = 8.73 \pm 0.04$. The difference relative to our value with the Holweger-Müller model atmosphere can be traced to differences in selected lines, adopted equivalent widths and much smaller non-LTE corrections (for completeness it should also be noted that Holweger uses intensity rather than flux profiles). In particular, Holweger adopts large H collision cross-sections, leading to small non-LTE abundance corrections. As described above, the evidence is stacked against such efficient H collisions. In addition, Holweger added “granulation corrections” amounting to -0.02 dex on average to the derived abundance, finally arriving at $\log \epsilon_{\text{O}} = 8.74 \pm 0.08$ when including the [O I] 630.0 nm line. It should be noted, however, that these granulation corrections represent the difference in derived abundances between full 2D spectrum synthesis calculations and corresponding 1D computations using the 1D average of the 2D model atmosphere (Steffen & Holweger 2002). Thus, the abundance corrections are designed to only reflect the effect of temperature inhomogeneities but not the difference in mean temperature structure with for example the Holweger-Müller model atmosphere. As

a consequence, these granulation corrections can differ significantly both in magnitude and sign from those estimated by our method, which also includes the effects of different mean temperature structures between the 1D and 3D models. As our 3D solar model atmosphere has successfully passed a range of observational tests (e.g. Stein & Nordlund 1998; Rosenthal et al. 1999; Asplund et al. 2000b; Asensio Ramos et al. 2003), we are confident that our approach is fully justified.

6. Conclusions

We have presented a determination of the solar oxygen abundance from an analysis of [O I], O I, OH vibration-rotation and OH pure rotation lines by means of a realistic time-dependent 3D, hydrodynamical model of the solar atmosphere. All oxygen indicators yield very consistent results, in marked contrast with studies employing classical 1D model atmospheres. The here derived solar oxygen abundance of $\log \epsilon_{\text{O}} = 8.66 \pm 0.05$ (Table 4) is significantly smaller than previously thought: the revision amounts to almost a factor of two (0.27 dex) compared with the often quoted value of $\log \epsilon_{\text{O}} = 8.93$ from Anders & Grevesse (1989), and still much smaller than the value of 8.83 recommended more recently by Grevesse & Sauval (1998). This low abundance is strongly supported by the excellent agreement between abundance indicators of very different temperature sensitivities and line formation depths, and between the observed and predicted line shapes and center-to-limb variations. It should be noted that not the whole difference with previous results is attributed to the employment of a 3D model atmosphere over classical 1D models since the adoption of more recent gf -values, more realistic non-LTE procedures, better observations and a proper accounting of blends also play an important role in this respect.

The new low solar oxygen abundance derived with the new generation of 3D hydrodynamical model atmospheres (e.g. Stein & Nordlund 1998; Asplund et al. 1999, 2000b; Asplund & García Pérez 2001) resolves the problematic high metallicity of the Sun compared with the solar neighborhood suggested by previous studies. The oxygen abundance presented here ($\text{O}/\text{H} = 460 \pm 50 \cdot 10^{-6}$) is in very good agreement with that measured in the local interstellar medium for realistic gas-to-dust ratios (Meyer et al. 1998; André et al. 2003): $\text{O}/\text{H} = 410 \pm 60 \cdot 10^{-6}$. In addition, the solar oxygen abundance is now similar to those obtained from studies of nearby B stars (Cunha & Lambert 1994; Kilian et al. 1994). The most recent collation suggests that the mean B star value is $\text{O}/\text{H} = 350 \pm 130 \cdot 10^{-6}$ (Sofia & Meyer 2001) but there is a significant scatter between the existing B star analyses. Given the uncertainties we do not consider the remaining differences with our new solar oxygen abundance as significant. Finally, our value is close to those of nearby young, Galactic disk F and G dwarfs: $\text{O}/\text{H} = 450 \pm 160 \cdot 10^{-6}$ (Sofia & Meyer 2001). Interestingly, while the previous discrepancy most often has been blamed on flaws in the analyses of hot stars and nebulae, the most serious shortcoming has apparently rather been on the solar side. We believe that 3D line formation calculations of late-type stars such as those presented herein finally address

this important issue, promising much more accurate abundance analyses for the future.

There is, however, at least one area where the new solar O abundance together with the corresponding downward revisions of the photospheric C, N and Ne abundances (Asplund 2003, 2004; Asplund et al. 2004b,c) does not resolve a problem but rather severely aggravates it. The accurate measurement of the solar oscillations, helioseismology, allows a unique glimpse of the structure of the solar interior (Christensen-Dalsgaard 2002). The analysis can be posed as an inversion problem, enabling the extraction of the variation of the sound speed with depth in the Sun. The predictions from standard models of the solar structure and evolution show a remarkable agreement with the observed sound speed from helioseismology to within $\Delta c_s/c_s = 4 \cdot 10^{-3}$ (e.g. Christensen-Dalsgaard 2002). The existing inversions are normally based on the opacities computed with the old Anders & Grevesse (1989) solar chemical composition, or at least compositions with much larger values than our new results. With the new significant down-ward revisions of the solar C, N, O and Ne abundances, the overall solar metallicity in the photosphere decreases from $Z_{\text{old}} = 0.0194$ (Anders & Grevesse 1989) to $Z_{\text{new}} = 0.0126$ (mass fraction of elements heavier than He). This diminished metallicity propagates to a significant modification of the opacity because C, N, O and Ne are main contributors to the opacity in different layers below the convection zone, and the sound speed is therefore directly affected. As a result, the excellent agreement between the predicted and observed sound speed variation with depth deteriorates markedly (Pijpers 2002, private communication; see also Boothroyd & Sackmann 2003). We note that the new solar chemical composition should also affect the determination of the solar He abundance in the outer convective zone from helioseismology inversion due to modifications of the standard solar model. Likewise, the initial He abundance in the protosolar cloud will likely be slightly smaller than the value $Y = 0.27$ (mass fraction of He) normally derived with existing solar evolution models based on the old metal abundances.

At this stage it is unclear whether a resolution to this problem can be found and if so where the solution may lay. In the meantime, we offer the tentative suggestion that the problem may be traced to the fact that the here obtained solar C, N and O abundances only refer to the photospheric values rather than the abundances found in the solar interior. If the diffusion of metals, as incorporated into the stellar evolution models used for the solar inversion, is more efficient than currently thought, it is conceivable that the good correspondence in terms of the sound speed variation could be recovered. The metallicity in the interior would then be significantly higher than that of the convection zone and the photosphere. The excellent concordance between all the different C, N and O diagnostics achieved with the new generation of 3D hydrodynamical solar model atmospheres in contrast with 1D analyses certainly strongly argues for that the metallicity of the solar photosphere is indeed significantly lower than previously thought.

Acknowledgements. MA has been supported by research grants from the Swedish Natural Science Foundation, the Royal Swedish

Academy of Sciences, the Göran Gustafsson Foundation, and the Australian Research Council. CAP gratefully acknowledges support from NSF (AST-0086321) and NASA (ADP02-0032-0106 and LTSA02-0017-0093). NG is grateful to the Royal Observatory (Brussels) for financial support. We wish to thank Mats Carlsson, Remo Collet, Ana Elia García Pérez, David Lambert, Arlette Noels, Åke Nordlund, Frank Pijpers, Bob Stein and Regner Trampedach for many helpful discussions and fruitful collaborations. We also thank Joan Vandekerckhove for his help with the calculations at the Royal Observatory (Brussels). NSO/Kitt Peak FTS data used here were produced by NSF/NOAO. The GCT was operated by the Universitäts/Sternwarte Göttingen at the Spanish Observatorio del Teide of the Instituto de Astrofísica de Canarias. We have made extensive use of NASA ADS Abstract Service.

References

- Allende Prieto, C., Asplund, M., García López, R.J., & Lambert, D.L. 2002a, *ApJ*, 567, 544
- Allende Prieto, C., Hubeny, I., & Lambert, D.L. 2003, *ApJ*, 591, 1192
- Allende Prieto, C., Lambert, D.L., & Asplund, M. 2001, *ApJ*, 556, L63
- Allende Prieto, C., Lambert, D.L., & Asplund, M. 2002b, *ApJ*, 573, L137
- Altrock, R.C. 1968, *Sol. Phys.*, 5, 260
- Anders, E., & Grevesse, N. 1989, *Geochim. Cosmochim. Acta*, 53, 197
- André, M.K., Oliveira, C.M., Howk, J.C., et al. 2003, *ApJ*, 591, 1000
- Anstee, S.D., & O'Mara, B.J. 1995, *MNRAS*, 276, 859
- Asensio Ramos, A., Trujillo Bueno, J., Carlsson, M., & Cernicharo, J. 2003 *ApJ*, 588, L61
- Asplund, M. 2000, *A&A*, 359, 755 (Paper III)
- Asplund, M. 2003, in: *CNO in the Universe*, Charbonnel C., Schaerer D., Meynet G. (eds.), ASP conference series 304, in press [astro-ph/0302409]
- Asplund, M. 2004, *A&A*, in press (Paper V)
- Asplund, M., & García Pérez, A.E. 2001, *A&A*, 372, 601
- Asplund, M., Carlsson, M., & Botnen, A.V. 2003a, *A&A*, 399, L31
- Asplund, M., Grevesse, N., Sauval, A.J., Allende Prieto, C., & Blomme, R. 2004b, to be submitted to *A&A* (Paper VI)
- Asplund, M., Grevesse, N., Sauval, A.J., Allende Prieto, C., & Blomme, R. 2004c, to be submitted to *A&A* (Paper VII)
- Asplund, M., Gustafsson, B., Kiselman, D., & Eriksson, K. 1997, *A&A*, 318, 521
- Asplund, M., Ludwig, H.-G., Nordlund, Å., & Stein, R.F. 2000a, *A&A*, 359, 669
- Asplund, M., Nordlund, Å., Trampedach, R., & Stein, R.F. 1999a, *A&A* 346, L17
- Asplund, M., Nordlund, Å., Trampedach, R., Allende Prieto, C., & Stein, R.F. 2000b, *A&A*, 359, 729 (Paper I)
- Asplund, M., Nordlund, Å., Trampedach, R., & Stein R.F. 2000c, *A&A*, 359, 743 (Paper II)
- Asplund, M., Nordlund, Å., & Trampedach, R. 1999b, in: *Theory and tests of convection in stellar structure*, Gimenez A., Guinan E.F., Montesinos B. (eds.), ASP Conf. series 173, p. 221
- Barklem, P.S., Belyaev, A., & Asplund, M. 2003, *A&A*, 409, L1
- Barklem, P.S., & O'Mara, B.J. 1997, *MNRAS*, 290, 102
- Barklem, P.S., O'Mara, B.J., & Ross, J.E. 1998, *MNRAS*, 296, 1057
- Belyaev, A., Grosser, J., Hahne, J., & Menzel, T. 1999, *Phys. Rev. A*, 60, 2151
- Blatherwick, R.D., Murcray, F.J., Murcray, F.H., Goldman, A., & Murcray, D.G. 1982, *Applied Optics*, 21, 2658
- Boothroyd, A.I., & Sackmann, I.J. 2003, *ApJ*, 583, 1004

- Botnen, A.V. 1997, Cand. Sci. Thesis, University of Oslo
- Botnen, A.V., & Carlsson, M. 1999, in *Numerical astrophysics*, Miyama S.M., Tomisaka K., Hanawa T. (eds.), p. 379
- Brault, J., & Neckel, H. 1987, *Spectral atlas of solar absolute disk-averaged and disk-center intensity from 3290 to 12510 Å*
- Carlone, C., & Dalby, F.W. 1969, *Can. J. Phys.*, 47, 1945
- Carlsson, M. 1986, *Uppsala Astronomical Observatory Report No. 3*
- Christensen-Dalsgaard, J. 2002, *Reviews of Modern Physics*, 74, 1073
- Cunha, K., & Daflon, S. 2003, in: *CNO in the Universe*, Charbonnel C., Schaerer D., Meynet G. (eds.), ASP Conf. series 304, in press
- Cunha, K., & Lambert, D.L. 1994, *ApJ*, 426, 170
- Delbouille, L., Neven, L., & Roland, G. 1973, *Photometric atlas of the solar spectrum from λ 3000 to λ 10000*, Institut d'Astrophysique, Université de Liège
- Drawin, H.W. 1968, *Z. Phys.*, 211, 404
- Farmer, C.B. 1994, "The ATMOS solar atlas", in: *Infrared Solar Physics*, Rabin D.M., Jefferies J.T. and Lindsey C. (eds), Kluwer, Dordrecht, p. 511
- Farmer, C.B., & Norton, R.H. 1989, "A high-resolution atlas of the infrared spectrum of the Sun and the Earth atmosphere from space: Vol. I The Sun", *Nasa Ref. Publ.* 1224
- Fleck, I., Grosser, J., Schnecke, A., Steen, W., & Voigt H. 1991, *J. Phys. B*, 24, 4017
- Goldman, A., Murcray, F.J., Gillis, J.H., & Murcray, D.G. 1981, *ApJ*, 248, L133
- Goldman, A., Murcray, D.G., Lambert, D.L., & Dominy, J.F. 1983, *MNRAS*, 203, 767
- Goldman, A., Schoenfeld, W.G., Goorvitch, D., et al. 1998, *JQSRT*, 59, 453
- Grevesse, N., Sauval, A.J., & van Dishoeck, E.F. 1984, *A&A*, 141, 10
- Grevesse, N., & Sauval, A.J. 1998, in: *Solar composition and its evolution – from core to corona*, Frölich C., Huber M.C.E., Solanki S.K., von Steiger R. (eds). Kluwer, Dordrecht, p. 161 (also *Space Sci. Rev.* 85, 161, 1998)
- Grevesse, N., & Sauval, A.J. 1999, *A&A*, 347, 348
- Gustafsson, B., Bell, R.A., Eriksson, K., & Nordlund, Å. 1975, *A&A*, 42, 407
- Hinkle K.H., & Lambert, D.L. 1975, *MNRAS*, 170, 447
- Holweger, H. 2001, in: *Solar and galactic composition*, Joint SOHO/ACE workshop, Wimmer-Schweingruber R.F. (ed.). AIP conference proceedings 598, p. 23
- Holweger, H., & Müller, E.A. 1974, *Sol. Phys.*, 39, 19
- Johansson, S., Litzén, U. Lundberg, H., & Zhang, Z. 2003, *ApJ*, 584, L107
- Kilian-Montenbruck, J., Gehren, T. & Nissen, P.E. 1994, *A&A*, 291, 757
- Kiselman, D. 1991, *A&A*, 245, L9
- Kiselman, D. 1993, *A&A*, 275, 269
- Kiselman, D. 1997, *ApJ*, 489, L107
- Kiselman, D. 2001, *New Astronomy Reviews*, 45, 559 [astro-ph/0010300]
- Kiselman, D., & Asplund, M. 2001, in *ASP Conf. Ser.* 223, *Cool stars, stellar systems and the Sun*, García López R.J. et al. (eds.), p. 684
- Kiselman, D., & Nordlund, Å. 1995, *A&A*, 302, 578
- Kneer, F., Schmidt, W., Wiehr, E., & Wittmann, A.D. 1987, *Mitteilungen der Astronomischen Gesellschaft*, 68, 181
- Kupka, F., Piskunov, N.E., Ryabchikova, T.A., Stempels, H.C., & Weiss, W.W. 1999, *A&AS*, 138, 119
- Kurucz, R.L. 1993, CD-ROM, private communication
- Kurucz, R.L., Furenlid, I., Brault, J., & Testerman, L. 1984, *Solar Flux Atlas from 296 to 1300nm*, National Solar Observatory, Sunspot, New Mexico
- Lambert, D.L. 1968, *MNRAS*, 138, 143
- Lambert, D.L. 1978, *MNRAS*, 182, 249
- Litzén, U., Brault, J.W., & Thorne, A.P. 1993, *Phys. Scr.*, 47, 628
- Mélen, F., Sauval, A.J., Grevesse, N., et al. 1995, *J. Molec. Spectrosc.*, 174, 490
- Meyer, D.M., Jura, M., & Cardelli, J.A. 1998, *ApJ*, 493, 222
- Mihalas, D., Däppen, W., & Hummer, D.G. 1988, *ApJ*, 331, 815
- Müller, E., Baschek, B., & Holweger, H. 1968, *Sol. Phys.*, 3, 125
- Nelson D.D. Jr., Schiffman, A., & Nesbitt, D.J. 1990, *J. Chem. Phys.*, 93, 7003
- Nissen, P.E., Primas, F., Asplund, M., & Lambert, D.L. 2002, *A&A*, 390, 235
- Nordlund, Å. 1982, *A&A*, 107, 1
- Piskunov, N.E., Kupka, F., Ryabchikova, T.A., Weiss, W.W., & Jeffery, C.S. 1995, *A&AS*, 112, 525
- Reames, D.V. 1999, *Space Sci. Rev.* 90, 413
- Reetz, J. 1998, PhD thesis, Ludwig-Maximilians Univ.
- Rolleston, W.R.J., Smartt, S.J., Dufton, P.L., & Ryans, R.S.I. 2000, *A&A*, 363, 537
- Rosenthal, C.S., Christensen-Dalsgaard, J., Nordlund, Å., Stein, R.F., & Trampedach, R. 1999, *A&A*, 351, 689
- Rosman, K.J.R., & Taylor, P.D.P. 1998, *Journal of Physical and Chemical Reference Data*, 27, 1275
- Sánchez Almeida, J., Asensio Ramos, A., Trujillo Bueno, J., & Chernicharo, J. 2001, *ApJ*, 555, 978
- Sauval A.J., & Tatum J.B. 1984, *ApJS*, 56, 193
- Sauval, A.J., Grevesse, N., Brault, J.B., Stokes, G.M., & Zander, R. 1984, *ApJ*, 282, 330
- Sedlmayr, E. 1974, *A&A*, 31, 23
- Sofia, U.J., & Meyer, D.M. 2001, *ApJ*, 554, L221
- Steffen, M., & Holweger, H. 2002, *A&A*, 387, 258
- Stein, R.F., & Nordlund, Å. 1998, *ApJ*, 499, 914
- Stein, R.F., & Nordlund, Å. 2001, *ApJ*, 546, 585
- Storey, P.J., & Zeippen, C.J. 2000, *MNRAS*, 312, 813
- Takeda, Y. 1994, *PASJ*, 46, 53
- Tomkin, J., Lemke, M., Lambert, D.L., & Sneden, C. 1992, *AJ*, 104, 1568
- Unsöld, A. 1955, *Physik der Sternatmosphären*, 2nd ed., Springer, Heidelberg
- Uitenbroek, H. 1998, *ApJ*, 498, 427

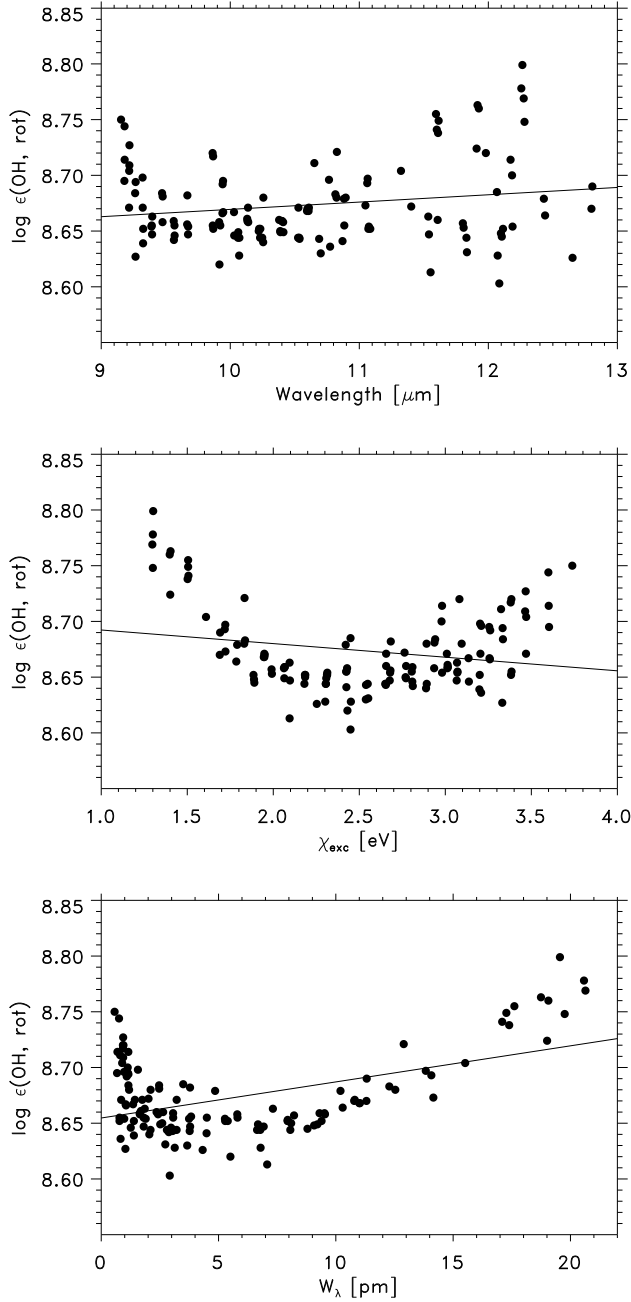


Fig. 10. The derived solar oxygen abundance from OH pure rotational lines using a 3D hydrodynamical solar model atmosphere as a function of wavelength, lower level excitation potential and line strength (in pm). The solid lines denote the least-square-fits. The rotational lines are more sensitive to the adopted microturbulence than the vibration-rotation lines since the stronger lines are partly saturated. The increased scatter for the weakest lines (which correspond to the highest excitation lines) is most likely due to increased observational difficulties in measuring the equivalent widths accurately

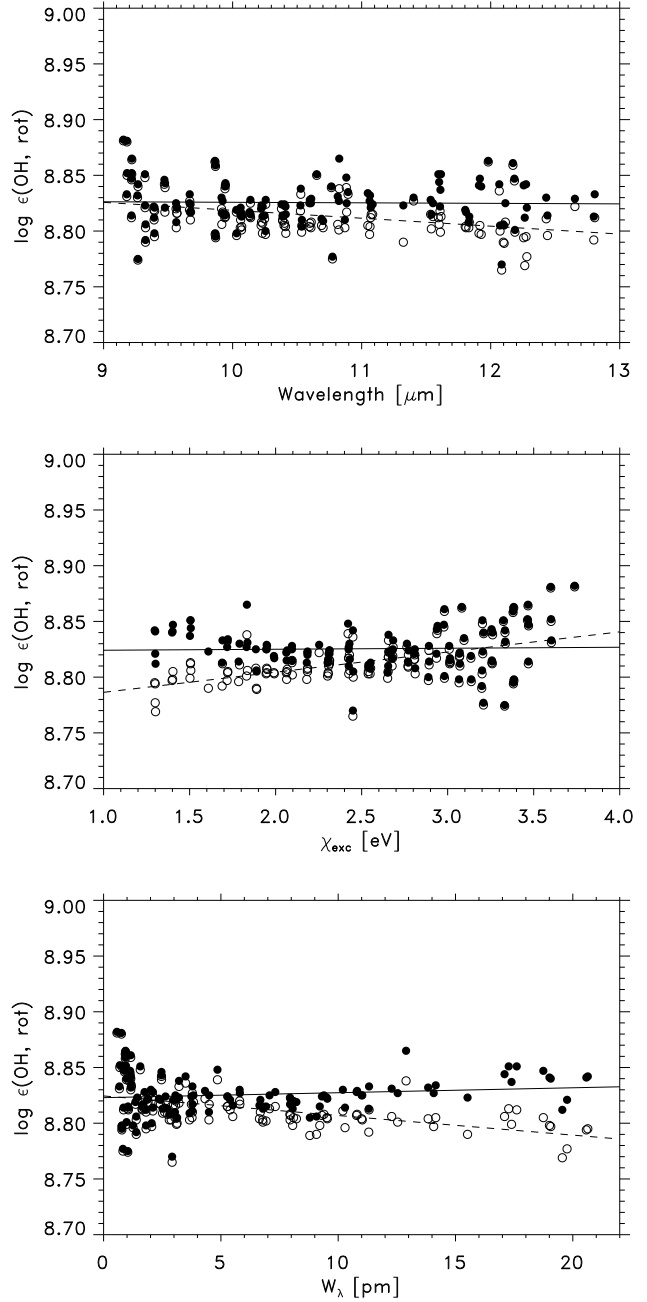


Fig. 11. Same as Fig. 10 but using the Holweger-Müller model atmosphere. The filled circles correspond to a microturbulence of $\xi_{\text{turb}} = 1.0 \text{ km s}^{-1}$ while the open circles are for $\xi_{\text{turb}} = 1.5 \text{ km s}^{-1}$ with the solid and dashed lines, respectively, denoting the least-square-fits

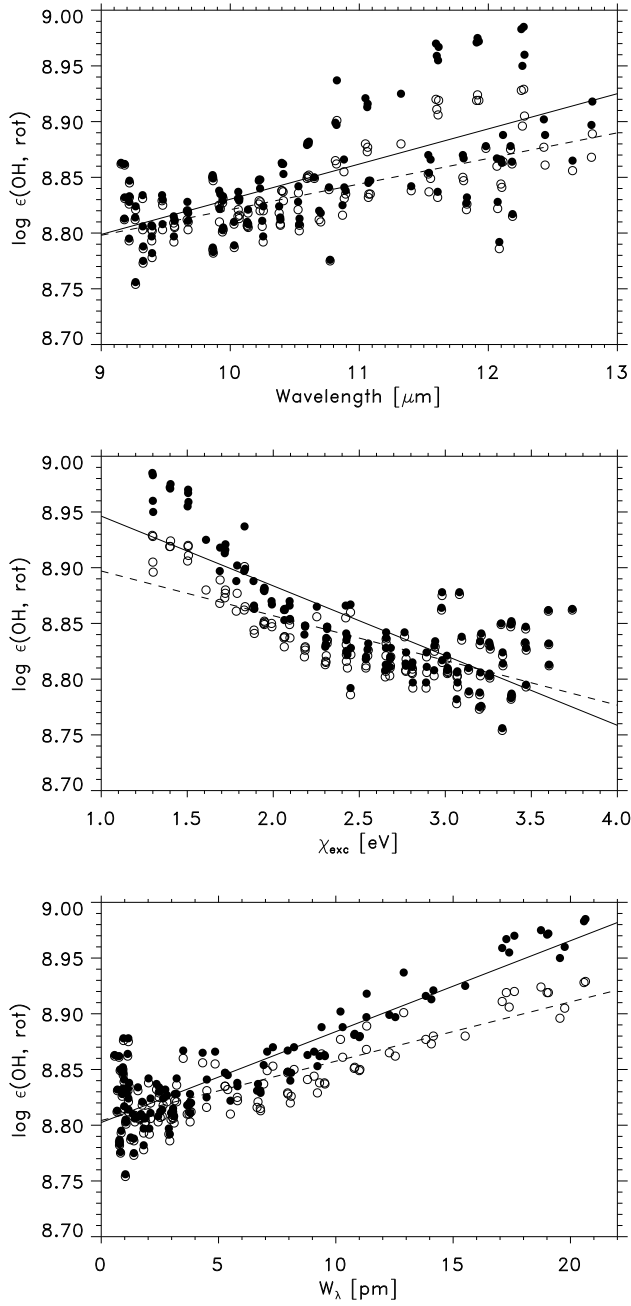


Fig. 12. Same as Fig. 10 but using a MARCS model atmosphere. The filled circles correspond to a microturbulence of $\xi_{\text{turb}} = 1.0 \text{ km s}^{-1}$ while the open circles are for $\xi_{\text{turb}} = 1.5 \text{ km s}^{-1}$ with the solid and dashed lines, respectively, denoting the least-square-fits